

Static and dynamic properties of shell-shaped condensates

Kuei Sun,^{1,*} Karmela Padavić,² Frances Yang,³ Smitha Vishveshwara,^{2,†} and Courtney Lannert^{3,4,‡}

¹*Department of Physics, The University of Texas at Dallas, Richardson, Texas 75080-3021, USA*

²*Department of Physics, University of Illinois at Urbana-Champaign, Urbana, Illinois 61801-3080, USA*

³*Department of Physics, Smith College, Northampton, Massachusetts 01063, USA*

⁴*Department of Physics, University of Massachusetts, Amherst, Massachusetts 01003-9300, USA*

Static, dynamic, and topological properties of hollow systems differ from those that are fully filled as a result of the presence of a boundary associated with an inner surface. Hollow Bose-Einstein condensates (BECs) naturally occur in various ultracold atomic systems and possibly within neutron stars but have hitherto not been experimentally realized in isolation on Earth because of gravitational sag. Motivated by the expected first realization of fully closed BEC shells in the microgravity conditions of the Cold Atomic Laboratory aboard the International Space Station, we present a comprehensive study of spherically symmetric hollow BECs as well as the hollowing transition from a filled sphere BEC into a thin shell through central density depletion. We employ complementary analytic and numerical techniques in order to study equilibrium density profiles and the collective mode structures of condensate shells hosted by a range of trapping potentials. We identify concrete and robust signatures of the evolution from filled to hollow structures and the effects of the emergence of an inner boundary, inclusive of a dip in breathing-mode-type collective mode frequencies and a restructuring of surface mode structure across the transition. By extending our analysis to a two-dimensional transition of a disk to a ring, we show that the collective mode signatures are an essential feature of hollowing, independent of the specific geometry. Finally, we relate our work to past and ongoing experimental efforts and consider the influence of gravity on thin condensate shells. We identify the conditions under which gravitational sag is highly destructive and study the mode-mixing effects of microgravity on the collective modes of these shells.

I. INTRODUCTION AND MOTIVATION

The realization of Bose-Einstein condensation in dilute ultracold atomic gases gave rise to spectacular directions in testing and exploring quantum phenomena at macroscopic scales [1–6]. Since the advent of this rich field, control and manipulation of these quantum fluids in diverse trapping potentials have yielded Bose-Einstein condensates (BECs) in a variety of geometries [7–18]. Here, we consider a fundamentally different geometry for a BEC—a hollow spherical shell. We theoretically study its evolution from a filled sphere to one having a small hollow region at its center to the thin spherical shell limit. Hitherto, creating hollow spheres has been an experimental challenge on Earth because of gravitational sag. Our study is particularly timely as a realization of a shell-shaped condensate [19, 20] is expected to take place within a “bubble trap” [21] under microgravity conditions in the space-based Cold Atomic Laboratory [22], recently launched to provide opportunities to investigate BEC behaviors that are unobservable in terrestrial laboratories [23].

A BEC in a shell-shaped geometry is fundamentally interesting from multiple perspectives: (i) Tuning between the filled sphere and thin shell limit offers a means of achieving dimensional cross-over from three-dimensional (3D) to two-dimensional (2D) behavior. We expect ther-

modynamics and collective mode properties to be acutely sensitive to dimensionality. (ii) The point at which the sphere initially hollows represents a change in topology. In contrast to other studies of topological transitions in quantum fluids, which require measuring Berry phases and related global invariants in momentum space, this topological change directly involves physical geometry. The filled and hollow spheres correspond to different second homotopy groups in that, unlike for the filled condensate, a spherical surface within the hollow BEC that surrounds its center cannot be continuously deformed into a point. (iii) The change in topology has physical consequences as it is accompanied by the appearance of a new, inner boundary. As we show here, the boundary has a marked effect on collective-mode structures. In terms of dimensional crossover and topological change, the hollowing out of the spherical BEC is a higher dimensional analog of BEC systems that have recently generated much interest upon their realization—annular and toroidal BECs [12, 13]. (iv) The shell BEC also offers noteworthy features that are not present in these geometries, such as vortex phenomena when subject to rotation and associated Kosterlitz-Thouless physics [24] on a curved, edgeless surface in the thin shell limit.

Shell-shaped BECs appear in a range of strongly correlated systems from the micron to the astronomical scale; the BEC studied here, being in isolation, provides the simplest such instance and thus acts as a test bed for more complex situations. As an established case, shell-shaped condensate regions occur in three-dimensional (3D) optical lattice systems of ultracold bosons [25–28], produced by the interplay between weak tunneling-to-

* kuei.sun@utdallas.edu

† smivish@illinois.edu

‡ clannert@smith.edu

interaction ratio (or strong lattice potential) [29–31] and inhomogeneous boson density due to harmonic confinement [32–34]. In the case of co-existing phases, superfluid (SF) regions are confined by surrounding Mott-insulator (MI) regions of the same bosons, creating an effective trapping potential [35, 36], rather than by an external trap. In addition, condensate shells are expected in Bose-Fermi mixtures [37–39], where a shell of Bose gas results from a phase separation from a core of fermions. At the astronomical scale, signals from neutron stars acting as radio pulsars have given rise to models that suggest the existence of macroscopic quantum states of matter, some possibly corresponding to shell crusts of neutron superfluids [40, 41].

In previous work [42], we presented preliminary evidence that a three-dimensional topological hollowing transition in a BEC should be accompanied by specific signatures in the collective mode spectra and illustrated these features using numerical solutions to the hydrodynamic equations for the specific case of the bubble-trap potential. In this work, we broaden and generalize the analysis of shell-shaped condensates and the hollowing transition, and directly address the experimental feasibility of detecting such a topological change. To that end, we use a family of trapping potentials (including the bubble trap) that can continuously tune between the filled sphere and the thin-shell limits. We perform an analysis of two concrete condensate properties—density profiles and collective mode structure, shown schematically in Fig. 1, and show that the two are intertwined during the topological transition in which the filled condensate becomes hollow. By employing a generalized trapping potential that allows us to adjust the density profile near the center of the BEC as it hollows, we are able to distinguish universal topological hollowing features in the collective mode spectra from those that are dependent on trap geometry. Thus, the work presented here provides a deeper understanding of physical mechanisms that result in signatures of the topological change in the shape of the BEC. Collective modes were the first phenomenon to be studied after the successful production of BECs and are well understood in the filled sphere case [43–56]; by taking the sphere as one limit in our family of BEC shapes, we show that the collective mode frequencies in the filled sphere and thin shell limits reflect the 3D and 2D limiting behaviors of the hollowing system. We additionally use an *in situ* numerical simulation of an experimental probe of collective modes to show that predicted hydrodynamic features in the spectra would in fact be relevant in experimental settings.

As our main results, we find that the crossover between the filled sphere and thin shell limits has several rich features and that the collective mode spectra in the system are excellent probes of the transition from filled to hollow geometry, in that: (i) the mode spectrum in the limiting case of the thin shell is significantly different from that of the filled sphere, which should be testable in the Cold Atom Laboratory (CAL) trap, (ii)

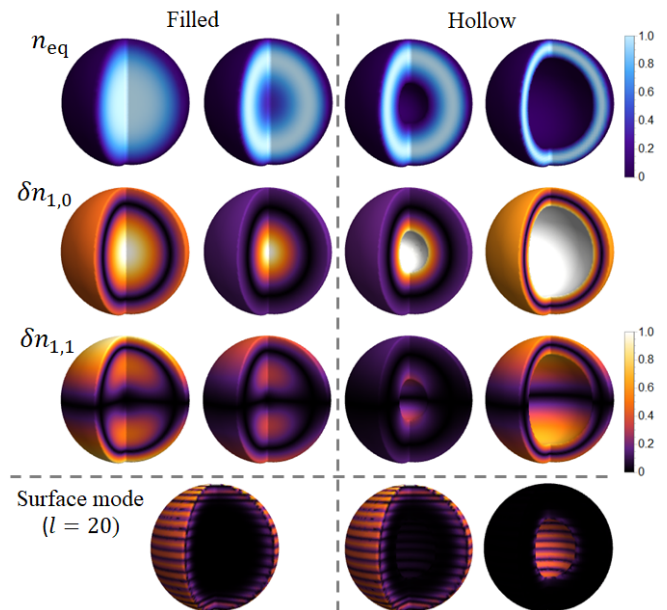


FIG. 1. (Color online) Top row: schematic equilibrium density profiles of a spherical BEC evolving from filled (left two panels) to hollow (right two) geometries. The middle two columns are close to the hollowing transition. Second and third rows: density deviation of collective modes $(\nu, \ell) = (1, 0)$ and $(1, 1)$, respectively, for the corresponding equilibrium density profile in the same column. Bottom row: density deviation of high angular momentum ($\ell = 20$) surface modes on a filled BEC (left, on the outer surface only) and a hollow BEC (right, on either the inner or outer surface). The density and density deviations are scaled by colors in the corresponding bar graph.

a dip in the frequency of breathing-type or radial collective modes (having nodes purely along the radial direction) accompanies the hollowing transition when an inner boundary first appears, (iii) a reconfiguration of the surface (high-angular-momentum) collective modes occurs at the hollowing transition, due to the appearance of the new surface. By employing a family of trapping potentials, we show that the dip feature is universal to the hollowing transition, but its sharpness depends on the details of how central condensate density depletes. Additionally, we identify features in the surface mode spectra that are specific to the hollowing in a bubble trap that would be absent for other trap geometries (such as the degeneracy in frequencies of modes localized at the inner and outer condensate shell surfaces, respectively). As the emergence of an additional boundary over the course of the hollowing-out deformation renders the filled sphere and the hollow shell condensates topologically distinct, our discussion identifies concrete, experimentally testable, features of a real-space topological transition.

Turning to the experimental realization of a shell condensate, this requires a combination of factors, all expected to be achieved in the near future. The bubble trap, first envisioned by Zobay and Garraway [21], relies

on radio-frequency (rf) dressing. Recently, the technique has been successfully used for double-well interferometry, ring-trap, and bubble-trap studies in one, two, and three dimensions, respectively [17, 57–63]. The 3D system can suffer sag due to the effect of gravity on the system. While previous experimental work with this geometry has so far been limited to the disk-shaped BEC produced under large gravitational sag [62, 63], a fully covered shell-shaped condensate may be produced in the presence of gravity if particular experimental parameters can be achieved. Alternately, the effects of gravity can be lessened by performing the experiment in microgravity. Two experimental microgravity facilities currently exist: the Zentrum für Angewandte Raumfahrttechnologie Und Mikrogravitation (ZARM) drop tower [64] in Bremen, Germany and NASA’s CAL aboard the International Space Station [22]. A series of experiments employing a bubble trap in the latter setting is expected to investigate the physics of closed BEC shells.

The role of gravity in the realization and behavior of BEC shells is thus significant. In addition to the gravity-free collective mode analysis, we therefore include the effects of gravity in two ways. First, we estimate the strength of gravity required to alter the BEC shell structure and show that typical strengths on Earth far surpass this limit. We also provide density profiles of shells in the presence of a gravitational field and show the sag effect. The effect, as a function of field strength, opens up the shell at a pole, altering the topology, and progresses to flatten the opened shell. Second, assuming microgravity conditions, we perturbatively analyze the effects of weak gravity on collective modes. As might be expected, the field breaks spherical symmetry, and modes differing by a unit of angular momentum in the spherically symmetric case become coupled.

Our comprehensive study of the evolution of a BEC from a filled sphere to a thin shell serves multiple purposes. It introduces a balance of analytic and numerical techniques appropriate for studying condensate equilibrium profiles and collective mode structures in hollow geometries. It presents concrete results for detecting a hollowing transition in such systems by pinpointing signatures in the BEC’s collective mode spectrum associated with the topological change of acquiring a new inner boundary. Appropriate to realistic settings, it assesses the effects of gravity and provides experimental estimates. We begin in Sec. II with a description of equilibrium properties of a BEC system in trapping potentials capable of evolving from a filled sphere to a thin shell as a function of an experimentally accessible tuning parameter. We incorporate a combination of techniques that best capture the associated BEC density profiles. We then introduce two techniques in Sec. III for studying dynamics using hydrodynamics in one case and numerical evolution following a sudden trap change in the other. In Sec. IV, we discuss the collective mode structures for the limiting cases of the well-known filled sphere as well as the thin shell. In Sec. V, we perform a thorough analy-

sis of the collective mode structure evolution between the limiting cases, first analyzing radially symmetric modes and then exploring higher angular momentum modes including surface modes. In Sec. VI, we show that features in the evolution of the collective mode spectra can be attributed to the hollowing of the condensate density at the center of the system. In Sec. VII, we turn to the presence of gravity, obtaining bounds for when the shell structure can be preserved in spite of a gravitational sag. We also perform a perturbative treatment of gravitational effects on the collective mode structure. We then end our exposition with considerations for realistic experimental settings in Sec. VIII and a conclusion in Sec. IX.

II. EQUILIBRIUM PROFILES

Here, we establish the equilibrium properties of hollow shell BECs upon which we build our collective mode description. We consider the limiting cases of a harmonic trap for the filled sphere geometry and a radially shifted harmonic trap for the thin shell condensate. A “bubble trap” proposed in the literature [21] and related to the experimental CAL trap can be tuned between these two limiting cases. We then consider a generalized trapping potential which can tune the condensate equilibrium density in the center of the system as it hollows, thereby allowing us to isolate the effect of density in the creation of an inner boundary. We analyze the equilibrium condensate density in these traps and note that the Thomas-Fermi approximation (which neglects the kinetic energy of the condensate) is a good approximation for many analyses, and pinpoints hollowing-out features by modeling sharp boundaries for the condensate. Since accounting for realistic condensate profiles and soft boundaries requires going beyond the Thomas-Fermi approximation, we also employ numerical methods for determining ground-state densities.

We describe the condensate wave function $\psi(\mathbf{r}, t)$ within the standard time-dependent Gross-Pitaevskii (GP) equation, given by

$$i\hbar\partial_t\psi(\mathbf{r}, t) = \left[-\frac{\hbar^2}{2m}\nabla^2 + V(\mathbf{r}) + U_0|\psi(\mathbf{r}, t)|^2 \right] \psi(\mathbf{r}, t), \quad (1)$$

where m is the particle mass, V is the trapping potential, and $U_0 = 4\pi\hbar^2 a_s/m$ is the interaction strength (proportional to the two-body scattering length a_s) [5]. In considering equilibrium properties, we employ the time-independent version of the GP equation obtained by assuming a condensate wavefunction of the stationary form $\psi(\mathbf{r}, t) = \psi(\mathbf{r})\exp(-i\mu t/\hbar)$, where μ is the chemical potential of the system. The equilibrium condensate density is then given by $n_{\text{eq}}(\mathbf{r}) = |\psi(\mathbf{r})|^2$.

A. Trapping potentials

We begin by defining trapping potentials that host the limiting cases of the filled spherical condensate and the thin condensate shell, and then discuss two possible trapping potentials for capturing the physics of the intermediate shell regime. Equilibrium density distributions of condensates are primarily determined by the trapping potential, with details such as their widths and maximum radii being influenced by the strength of interactions between the atoms. In the equations below, we adopt dimensionless length units, rescaled by an oscillator length $S_l = \sqrt{\hbar/(2m\omega)}$, where ω is a relevant frequency, for instance, of the bare harmonic confining trap prior to rf dressing.

As the simplest and best understood case, we consider the spherically symmetric harmonic trap, which produces a fully filled spherical condensate. The associated trapping potential takes the form

$$V_0(r) = \frac{1}{2}m\omega_0^2 S_l^2 r^2, \quad (2)$$

where ω_0 is the single-particle frequency of small oscillations and r is the dimensionless radial distance from the origin (spherical center).

In the opposite limit of a very thin spherical condensate shell, a simple trapping potential that would produce this shape is a radially shifted harmonic trap of the form,

$$V_{\text{sh}}(r) = \frac{1}{2}m\omega_{\text{sh}}^2 S_l^2 (r - r_0)^2, \quad (3)$$

where the location of potential minimum r_0 is nonzero, and ω_{sh} is the frequency of single-particle oscillations near this radius. Several salient features of the equilibrium density and collective mode structure of the thin shell limit are well captured by analyzing condensates in this radially shifted potential. In addition, this potential is a good approximation for any trapping potential with a radially shifted minimum in the thin shell limit.

However, the radially shifted harmonic potential is unphysical for situations where the condensate density is finite close to the trap center; the slope of the potential is discontinuous at $r = 0$. For a more realistic trap producing a hollow condensate, we consider a ‘‘bubble trap’’ [21, 62, 63], which has been recognized as a good candidate. Such a trap is achievable in the cold atomic setting by employing time-dependent, radio frequency induced adiabatic potentials within a conventional magnetic trapping geometry. Its form is given by

$$V_{\text{bubble}} = m\omega_0^2 S_l^2 \sqrt{(r^2 - \Delta)^2/4 + \Omega^2}, \quad (4)$$

where Δ and Ω are the effective (dimensionless) detuning between the applied rf-field and the energy states used to prepare the condensate and the Rabi coupling between these states, respectively. Note that the minimum of this potential is found at $r = \sqrt{\Delta}$ and the frequency of single-particle small oscillations around this minimum is $\sqrt{\Delta/\Omega}\omega_0$.

The parameters Δ and Ω together allow for tuning between the filled condensate and the thin shell. When $\Delta = \Omega = 0$, the bubble-trap potential reduces to a harmonic trap with frequency ω_0 . For large Δ , it is approximated near its minimum by a radially shifted harmonic trap [Eq. (3)] with frequency $\omega_{\text{sh}} = \sqrt{\Delta/\Omega}\omega_0$. Slowly increasing or decreasing the trap parameter Δ results in a continuous deformation between the two limiting geometries of a filled sphere and a thin spherical shell.

While the change from a filled to a hollow system is topological in nature (an inner surface is created), because condensates have continuous density profiles, the hollowing in a real system will be gradual. The density at the center becomes smaller until it is effectively zero. One of the main questions addressed in this work is the following: What are the signatures of this transition in the collective mode spectrum of the system?

In order to tune the detailed behavior of the condensate density during the hollowing transition, we also consider the following general radially shifted trapping potential

$$V_{\text{gt}}(r) = \frac{1}{2}m\omega_{\text{gt}}^2 R^2 S_l^2 \left[\left(\frac{r}{R} \right)^\alpha - \gamma \right]^2, \quad (5)$$

where R represents the (dimensionless) characteristic size of the system (or exactly the outer sharp boundary under the Thomas-Fermi approximation). Here, $0 \leq \gamma \leq 1$ is a dimensionless parameter that tunes the radially shifted trap minimum for realizing the evolution between filled sphere and thin shell, and α determines the polynomial growth of condensate density in the radial direction from the boundary. Note that the radially shifted harmonic trap of Eq. (3) is a special case of the general trap having $\alpha = 1$. In Sec. VI, we will use this general potential to understand the universal features of the collective-mode spectrum that occur as the system becomes hollow in the center.

B. Evolution of equilibrium density from filled sphere to thin shell

Having enumerated the trapping potentials used in our studies, we next find the equilibrium density profiles of condensates confined to these traps.

1. Thomas-Fermi approximation

In the limit of strong interactions the Thomas-Fermi approximation, in which the kinetic energy term in Eq. (1) is disregarded, is commonly used. In this approximation, the equilibrium density profile is given by

$$n_{\text{eq}}(\mathbf{r}) = \frac{V(\mathbf{R}) - V(\mathbf{r})}{U}, \quad (6)$$

where R is the outer radius of the condensate, $U = U_0 S_l^{-3}$, and the chemical potential is equal to $\mu = V(R)$. The strong interaction limit is defined by $Na_s/S_l \gg 1$

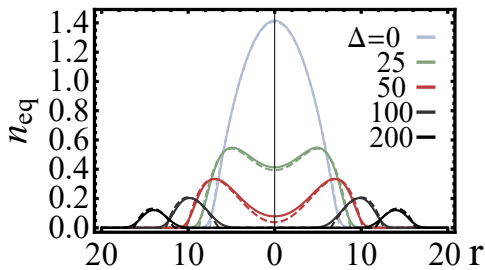


FIG. 2. (Color online) Ground-state density profiles $n_{\text{eq}}(r)$ in the bubble trap for $\Delta = 0$ (lighter blue curves), 25 (light green), 50 (dark red), 100 (darker gray), and 200 (black). The various values of Δ show the evolution from the spherical (filled) condensate in a harmonic trap at $\Delta = 0$ to a thin-shell condensate for large Δ (the 3D visualization can be found in the top row of Fig. 1). The solid (dashed) curves are obtained from the numerical solution of the GP equation (the Thomas-Fermi approximation). Here, we use $\Delta/\Omega = 1$ and an interaction constant $u = 10,000$.

for N particles, where S_l is the characteristic length of the trapping potential defined in Sec. II A.

Within this approximation, the condensate density $n_{\text{eq}}(\mathbf{r})$ and boundary $n_{\text{eq}}(\mathbf{R}) = 0$ are determined by the trap geometry and the total number of particles $N = \int n_{\text{eq}}(\mathbf{r}) d\mathbf{r}$. This approximation can be used to show that a BEC in the bubble trap with a slowly changing detuning Δ transitions from a filled sphere to a hollow shell when $\Delta = R^2/2$ (where we have set $\Delta = \Omega$ for convenience).

2. Beyond Thomas-Fermi

A more accurate numerical solution for the ground state of the GP equation (for any value of interaction strength) can be found using an imaginary-time algorithm [65]. In Fig. 2, we show the evolution of the numerical ground state in the bubble trap as the detuning Δ is varied from 0 to 200 (corresponding to evolution from a filled, harmonically trapped, sphere to a thin spherical shell) with $\Delta/\Omega = 1$ fixed. The equilibrium density given by the Thomas-Fermi approximation is shown for comparison. While for the most part the density profiles match each other, those found through the exact numerical calculation show a more realistic, smooth decrease in density at the edges of the condensate.

We note that for intermediate interaction strength U , the relative interaction energy (as measured by the ratio of $\frac{U_0}{2} \int |\psi|^4 d\mathbf{r}$ to the total energy) can decrease considerably as one moves from a filled sphere to a thin shell when the number of trapped particles N is kept fixed. This is due to the large decrease in maximum particle density $n = |\psi|^2$ as the shell becomes thin. In order to compare with results of the Thomas-Fermi approximation in the thin shell limit, we have used a relatively large value of dimensionless interaction strength

$u = 8\pi N a_s / S_l = 10,000$ in our numerics, where S_l is the oscillator length for the harmonic trap when $\Delta = 0$. For ^{87}Rb and a bare trap frequency of 10–100 Hz, for instance, this corresponds to $N = 2 \times 10^5$ to 5×10^4 atoms.

Taking into account the analyses and arguments above, in what follows, we either employ the Thomas-Fermi approximation or the numerical ground state, as appropriate.

III. METHODS AND APPROACHES FOR DYNAMICS OF COLLECTIVE MODES

Having discussed the equilibrium behavior of a trapped condensate, in this section we consider its dynamics. In order to study the collective motions of spherically symmetric BECs we present four complementary methods appropriate in different regimes: (i) The first method uses a hydrodynamic approach combined with Thomas-Fermi equilibrium density profiles, which leads to a differential eigenvalue problem for all possible collective motions of small density deviations of a given condensate geometry. This method provides a good approximation for collective mode spectra in any spherically symmetric trap. (ii) Second, we employ a fully numerical approach that mimics the experimental excitation of collective oscillations through sudden changes in trap potential. While more realistic, this method can only capture low-lying collective modes due to finite resolution. (iii) A hybrid method uses the hydrodynamic equations, but applied to the numerical ground-state density and has the advantages of the simpler Thomas-Fermi hydrodynamic approach, but with realistic treatment of the condensate boundaries. (iv) A fourth method focuses on surface modes localized to the boundary of the system by linearizing the hydrodynamic eigenproblem close to the boundaries of the condensate.

A. Hydrodynamic treatment

Here, we describe the condensate's collective dynamics in terms of hydrodynamic density oscillations. The small density fluctuation $\delta n(\mathbf{r}, t)$ out of the equilibrium condensate density $n_{\text{eq}}(\mathbf{r})$ is described by the standard hydrodynamic equation of motion (see details in Refs. [5, 46]),

$$m S_l^2 \partial_t^2 \delta n = U \nabla \cdot (n_{\text{eq}} \nabla \delta n) + O(\delta n^2, \partial^3 \delta n, \partial^2 n_{\text{eq}}). \quad (7)$$

We will use this expression for specific trap geometries under a number of assumptions about the nature of the collective modes. First, the nonlinear terms of δn are negligible when we assume that deviations away from the equilibrium density are small, i.e., the amplitude of the collective mode oscillations is small. Furthermore, the higher derivatives of δn are negligible if the oscillations in the condensate density are smooth, i.e., δn varies only on length scales much larger than the local coherence length

$a_d\sqrt{a_d/a_s}$ where a_d is the interparticle spacing [5]. The second derivative of n_{eq} , associated with the kinetic energy arising from the density variation due to the trap, is also negligible in the strong interaction (Thomas-Fermi) limit.

Assuming normal-mode oscillations $\delta n(\mathbf{r}, t) = \delta n(\mathbf{r})e^{i\omega t}$, Eq. (7) takes the form,

$$-\frac{mS_t^2}{U}\omega^2\delta n = \nabla n_{\text{eq}} \cdot \nabla\delta n + n_{\text{eq}}\nabla^2\delta n. \quad (8)$$

The eigenvalues and eigenfunctions satisfying this expression correspond to collective modes with oscillation frequencies ω and profiles $\delta n(\mathbf{r})$, respectively. We note that this expression shows that the hydrodynamic approach can be applied for any equilibrium density profile. While for the most part we will use the density obtained from the Thomas-Fermi approximation, we will use the numerical ground-state density found from the imaginary-time algorithm for comparison.

For traps with spherical symmetry, we can decompose $\delta n(\mathbf{r}) = D(r)Y_{\ell m_\ell}(\theta, \varphi)$, where $Y_{\ell m_\ell}$ are the usual spherical harmonics and find that Eq. (8) reduces to

$$\frac{mS_t^2}{U}\omega^2 r^2 D = -\frac{d}{dr} \left(r^2 n_{\text{eq}} \frac{dD}{dr} \right) + \ell(\ell+1)n_{\text{eq}}D. \quad (9)$$

Using the Thomas-Fermi equilibrium density profile of Eq. (6) the eigenproblem becomes

$$mS_t^2\omega^2 D = \frac{dV}{dr} \frac{dD}{dr} - [V(R) - V(r)] \times \left[\frac{dD^2}{dr^2} + \frac{2}{r} \frac{dD}{dr} - \frac{\ell(\ell+1)}{r^2} D \right]. \quad (10)$$

Equations (9) and (10) have analytic solutions in two limiting cases of filled sphere and thin shell, which are studied in Sec. IV, or can be analyzed with perturbation theory, as for the finite thin-shell case in Sec. IV B or for the gravity effects studied in Sec. VII B. In general, our eigenproblem is of the Sturm–Liouville form and can hence be treated with a finite-difference method, whose technical details are presented in Appendix A. Our hydrodynamic results for the evolution between filled sphere and hollow shell in Secs. V and VI are obtained from the finite-difference method.

1. Surface modes

Here, we highlight the case of collective modes localized near the edges of the condensate—its surface modes. Following the earlier work in Ref. [66], we note that in order to identify surface modes it is appropriate to expand the Thomas-Fermi equilibrium density profile about $\mathbf{r} = \mathbf{r}_b$ for $V(\mathbf{r}_b) = \mu$, the position of the condensate boundary. Consequently, the Thomas-Fermi equilibrium density profile can be expressed as

$$n_{\text{eq}}(\mathbf{r}) = \frac{\mathbf{F} \cdot (\mathbf{r} - \mathbf{r}_b)}{U}, \quad (11)$$

where $\mathbf{F} = -\nabla V(\mathbf{r}_b)$.

Denoting the direction of ∇V by x and the position of the boundary (which is a 2D equipotential surface) by $x = x_b$, we proceed to estimate the size of the region near the boundary within which this treatment of the condensate equilibrium density is reliable. Recalling that the Thomas-Fermi approximation follows from neglecting the contribution of the kinetic energy in the GP equation, Eq. (1), we estimate that kinetic energy dominates for $x_b - x \leq \delta_{\text{sm}}$ where

$$\delta_{\text{sm}} = \left(\frac{\hbar}{2m|\mathbf{F}|} \right)^{1/3}. \quad (12)$$

If the trapping potential varies slowly on the length scale δ_{sm} , it is then a good approximation to expand the potential and the Thomas-Fermi equilibrium density about $r = r_b$ as suggested above [5].

We next solve the hydrodynamic equations for the linearized potential $V(x) = Fx$ with x defined so that it vanishes at r_b . First, we note that in the y and z directions, defined relative to x , there is translational invariance so that a density oscillation $\delta n = \delta n(x, y, z)e^{-i\omega t}$ must correspond to a plane wave in these two variables. As in Ref. [66], we chose the z -direction as the direction of propagation of this collective mode and denote its wave number by q . Consequently, the collective motion only has x and z dependences and we can rewrite the hydrodynamic equation as

$$mS_t^2\omega^2\delta n(x, z) = F \frac{\partial\delta n(x, z)}{\partial x} + Fx \left[\frac{\partial^2\delta n(x, z)}{\partial x^2} + \frac{\partial^2\delta n(x, z)}{\partial z^2} \right]. \quad (13)$$

Solutions to this expression can take the form

$$\delta n(x, z) = f(qx)e^{qx+iqz} \quad (14)$$

for some smooth function $f(qx)$. We note that in this ansatz, the exponential factor in the variable x corresponds to an exponential decay away from the condensate boundary. We obtain the frequencies for modes described by Eq. (14) as

$$mS_t^2\omega_{\text{in,out}}^2 = (1 + 2\nu_{\text{in,out}})F_{\text{in,out}}q_{\text{in,out}}, \quad (15)$$

while the modes themselves are of the form

$$\delta n(x, y, z, t) = C_{\nu_{\text{in,out}}} L_{\nu_{\text{in,out}}}(-2q_{\text{in,out}}x) \times e^{q_{\text{in,out}}x + iq_{\text{in,out}}z - i\omega_{\text{in,out}}t},$$

where $C_{\nu_{\text{in,out}}}$ is the overall magnitude and $L_{\nu_{\text{in,out}}}$ are Laguerre polynomials. Here, indices $\nu_{\text{in,out}}$ count the number of radial nodes of a collective mode confined to a particular boundary surface of the condensate.

The specific behavior of surface modes, depending on the specific physical topology of the condensate, is further discussed in Sec. IV C for the limiting shell case and in Secs. VB and VIC for the evolution between filled sphere and hollow shell in the bubble and general traps, respectively.

B. Sudden quench numerics

While the hydrodynamic treatment described above is adequate for obtaining the collective mode spectrum, our numerical simulations serve as a good complement. They even capture physics beyond the hydrodynamic regime for the bubble trap geometry, which can access the filled sphere and thin shell limits as well as the evolution between them. Taking inspiration from experimental methods for exciting collective modes of trapped BECs [44], we theoretically probe the excitations of the system by direct simulation of the GP equation after a small and sudden change in the trap potential takes the system slightly out of equilibrium.

After first finding the numerical ground state of the GP equation describing a BEC confined by the bubble trap for one set of values of trap parameters Δ_0 and Ω_0 , we then time-evolve this initial state using the GP equation with different values of trap parameters Δ and Ω . This results in time-oscillating features in the time evolved condensate wavefunction $\psi(\mathbf{r}, t)$. The frequencies of these oscillations can be extracted by using a fast-Fourier transform in the time domain. For small changes ($\Delta_0 - \Delta \ll \Delta_0$ and likewise for Ω) these simulations should probe the linear response and low-lying modes of the system.

In practice, we use the explicit time-marching method of Ref. [67] to time evolve the initial numerical ground state (found in Sec. II B) for two types of quenches. In one case, we let $\Delta/\Omega \neq \Delta_0/\Omega_0$ change while keeping $\Delta = \Delta_0$ fixed, which fixes the mean radius of the shell but allows the tightness of the confinement to change. For a hollow shell, this quench is expected to primarily excite modes in which the thickness of the shell oscillates. Alternatively, we change $\Delta \neq \Delta_0$ while keeping $\Delta/\Omega = \Delta_0/\Omega_0$ fixed so that the tightness of the trap is constant while the mean radius of the shell varies. This method is found to more equally excite modes with both even and odd values of ν (which denotes the number of radial nodes in the collective mode). The two methods agree when the same mode frequencies are resolvable. Because these quenches both preserve spherical symmetry, they only probe spherically symmetric ($\ell = 0$) modes of the system. In principle, appropriate quenches could be designed to probe nonsymmetric states as well (such as an offset of the center of the trap in the x direction, resulting in excitation of the center-of-mass modes). In what follows, we concentrate on numerical resolution of the spherically symmetric modes only.

IV. COLLECTIVE MODES: LIMITING CASES

In this section, we apply the hydrodynamic approach of Sec. III A to a filled spherical condensate and a thin condensate shell. In this detailed treatment, we establish the full frequency spectrum and associated mode behaviors of these two limiting cases of our general hollowing

system. Because of the spherical symmetry of the system, the collective modes can be characterized by two quantum numbers: one for the number of radial nodes, ν , and one for the orbital angular momentum denoted by the index ℓ . We find that the presence of an inner boundary in condensate shells produces features that are not found in fully filled spherical BECs even for the same quantum numbers. These results not only provide a check for the full evolution between the limits when analyzing the bubble trap and other cases in subsequent sections, they also provide a better understanding of the intermediate crossover regime and corroborate predictions for this regime.

A. Filled sphere: Quadratic potential

We first recapitulate the results of hydrodynamic approach for the well-understood case of a condensate in a spherically symmetric harmonic trap, Eq. (2), $V_0 = \frac{1}{2}m\omega_0^2 S_l^2 r^2$. We assume the strong interaction regime where the Thomas-Fermi approximation is applicable.

Solving Eq. (10), one obtains [5, 46]

$$\omega_{\nu,\ell}^{\text{SP}} = \omega_0 \sqrt{\ell + 3\nu + 2\nu\ell + 2\nu^2}, \quad (16)$$

where ν is a radial index as above and ℓ is an index of the orbital angular momentum. We see from Eq. (16) that in addition to the trivial mode $\omega_{0,0}^{\text{SP}} = 0$, which corresponds to a uniform density deviation but does not physically exist in real systems, any nonzero mode has frequency $\omega_{\nu,\ell}^{\text{SP}} \geq \omega_0$. A schematic density deviation profile for $(\nu, \ell) = (1, 0)$ [(1, 1)] is presented in the leftmost panel of the second (third) row of Fig. 1. We see that ν and ℓ count the nodes, at which the density deviation vanishes, in radial and angular directions, respectively. The $\ell = 0$ modes exhibit only the radial expansion and contraction (spherically symmetric) and are referred as breathing modes. The $\ell = 1$ modes exhibit a center-of-mass oscillation between the southern and northern hemispheres and are referred as sloshing or dipole modes. The breathing, sloshing, and quadrupole ($\ell = 2$) modes have been experimentally observed [43, 44, 55, 56] to be in good agreement with the theoretical predictions.

B. Thin shell: Radially shifted quadratic potential

As discussed in Sec. II, the shell-shaped condensate can be realized by trapping in a radially shifted harmonic potential, Eq. (3),

$$V_{\text{sh}}(\mathbf{r}) = \frac{1}{2}m\omega_{\text{sh}}^2 S_l^2 (r - r_0)^2.$$

The potential minimum (or condensate density maximum) appears at $r = r_0$. Under the Thomas-Fermi approximation, given the shell's outer radius $R = R_{\text{out}} = r_0 + \delta$ and $\delta < r_0$, Eq. (6) yields the inner radius

$R_{\text{in}} = r_0 - \delta$. Here, the condensate shell has two distinct radii, R_{in} and R_{out} , in contrast to a single outer radius R for the fully filled spherical condensate. Evaluating the integral $N = \int n_{\text{eq}}(\mathbf{r}) d\mathbf{r}$, we find the relationship between the total number of particles, N , and the shell's dimensionless thickness, 2δ :

$$N = \frac{8\pi m \omega_{\text{sh}}^2 S_l^2}{3U} \delta^3 \left(r_0^2 + \frac{\delta^2}{5} \right). \quad (17)$$

If $\delta \ll r_0$, this reduces to

$$2\delta = \left(\frac{3UN}{\pi m \omega_{\text{sh}}^2 S_l^2 r_0^2} \right)^{1/3}. \quad (18)$$

We define the ‘‘thin shell limit’’ by $c \equiv r_0/\delta \gg 1$ and solve Eq. (10) for the collective modes in this limit.

We let $\eta = \frac{r-r_0}{\delta}$ (so $-1 \leq \eta \leq 1$), $\lambda = (\omega/\omega_{\text{sh}})^2$, as well as $y(\eta)/(\eta+c) = D(r)$ and express Eq. (10) as

$$\left[(1-\eta^2) \frac{d^2}{d\eta^2} - 2\eta \frac{d}{d\eta} + 2\lambda + \frac{2\eta}{\eta+c} - \ell(\ell+1) \frac{1-\eta^2}{(\eta+c)^2} \right] y = 0. \quad (19)$$

In the limit of a very thin shell ($c \rightarrow \infty$), we can ignore the last two terms in Eq. (19). The solutions are Legendre polynomials $y_\nu(\eta) = \sqrt{\frac{2\nu+1}{2}} P_\nu(\eta)$ having eigenfrequencies

$$\omega_{\nu,\ell}^{\text{sh}} = \omega_{\text{sh}} \sqrt{\nu(\nu+1)/2}. \quad (20)$$

Here, similar to the filled sphere case, the thin shell case has nonzero breathing mode frequencies higher than the characteristic trapping frequency. But in contrast to the filled case, all ℓ modes are nearly degenerate compared with the radial energy scale. The rightmost panel of second (third) row of Fig. 1 shows a schematic density deviation profile for $(\nu, \ell) = (1, 0)$ [(1, 1)], from which we see nodal structures similar to the filled sphere case. For a very thin shell, however, the energy associated with a collective mode is largely unaffected by the number of angular nodes. In other words, the radial behavior of the collective mode determines its eigenfrequency. We note that this degeneracy of ℓ modes has previously been shown [68] to characterize the collective modes of thin ring-shaped BECs as well. Additionally, we note that, unlike the indices $\nu_{\text{in,out}}$ of Eq. (15), ν denotes the number of radial zeros of a collective mode spanning the full extent of the condensate shell.

For a slightly thicker shell in which c deviates from the infinite limit, we calculate the correction to $\omega_{\nu,\ell}^{\text{sh}}$ by treating the last two terms in Eq. (19) perturbatively. We obtain

$$\left(\frac{\omega_{\nu,\ell}^{\text{sh}}}{\omega_{\text{sh}}} \right)^2 = \frac{\nu(\nu+1)}{2} \left[1 + \frac{4c^{-2}}{(2\nu-1)(2\nu+3)} \right] + \frac{c^{-2}\ell(\ell+1)}{4} \left[1 - \frac{1}{(2\nu-1)(2\nu+3)} \right]. \quad (21)$$

The leading corrections to the frequency are of the order $O(c^{-2})$. In a shell with a large but finite c , the frequency spectrum of the lowest lying collective modes (low ν and ℓ indices) has the form of bands corresponding to different ν separated by $O(\omega_{\text{sh}})$, with each band having fine levels corresponding to different ℓ separated by $O(c^{-2}\omega_{\text{sh}})$. As a result, the two energy scales for radial and angular motions are well separated in a thin shell. As the thickness of the shell increases, the effects of the angular oscillations on its collective mode frequency and energy become more prominent.

In the $\nu = 0$ case, we obtain purely angular collective modes

$$\omega_{0,\ell}^{\text{sh}} = c^{-1} \omega_{\text{sh}} \sqrt{\ell(\ell+1)/3}. \quad (22)$$

Accordingly, we expect the collective modes of a very thin shell that do not have any radial nodes to correspond to very low (but still nonzero) frequencies. Such low-frequency excitations (compared with the trap frequency) do not exist in the filled-sphere condensate.

Additionally, we note that the presence of an inner boundary for a shell condensate can have important effects on its collective modes. In the limit of large ℓ ($\gg c$), the term $\ell(\ell+1)(1-\eta^2)/(\eta+c)^2$ in Eq. (19) dominates. This term behaves as a potential barrier between the inner and outer boundaries $\eta = \pm 1$, respectively, and favors low-frequency modes localizing on either the inner or outer shell surface (potential minimum). This is different from the filled-sphere condensate, which does not have an inner boundary. We proceed to discuss these surface modes below, and later in Sec. VB, we show how this effect causes a sudden change in the spectrum of large ℓ modes as a bubble-trap system evolves from a sphere to a shell.

C. Surface modes

Noting that the most striking difference between a fully filled spherical BEC and a hollow condensate shell is the presence of an additional, inner boundary for the latter, we employ the techniques presented in Sec. III A in order to study the collective modes localized at condensate boundaries.

For the collective modes localized at the outer edge of the fully filled spherical BEC it is known that [66]

$$\omega_{\nu,\ell}^{\text{sp}} = \omega_0 \sqrt{\ell(2\nu+1)}. \quad (23)$$

In presenting this result, we note that this expression is exactly the large $\ell \gg 1$ limit of the collective mode frequencies given by Eq. (16).

To study the modes confined to the inner and outer surfaces of the hollow condensate shell we first consider the radially shifted quadratic potential of trapping frequency ω_{sh} in Eq. (3) and obtain

$$mS_l^2 \omega_{\text{in,out}}^2 = (1 + 2\nu_{\text{in,out}}) F_{\text{in,out}} q_{\text{in,out}}, \quad (24)$$

or, more precisely,

$$\omega_{\text{in,out}}^{\text{sh}} = \omega_{\text{sh}} \sqrt{\ell(1 + 2\nu_{\text{in}}) \frac{|R - r_0|}{r_{\text{in,out}}}}, \quad (25)$$

where we identify the wave numbers $q = \ell/r_{\text{in,out}}$ and calculate $r_{\text{in}} = 2r_0 - R$ and $F_{\text{in,out}} = \pm\omega_{\text{sh}}^2(R - r_0)$. We note that collective modes on the inner surface have a higher frequency, for the same number of radial and angular nodes (ν and ℓ), than those on the outer surface. Recalling that the radially shifted trapping potential captures the salient characteristics of thin BEC shell dynamics, we note that these expressions are only representative of condensate behavior for $r_0 \approx R$. This implies that in the thin shell limit, where the areas of the inner and the outer boundary are comparable, frequencies of surface modes hosted on either are nearly equivalent as well. At the same time, we note that this analysis is only applicable to shells of thickness $\delta > 2\delta_{\text{sm}}$ as in thinner condensate shells the kinetic energy near the condensate boundaries cannot be neglected [recall Eq. (12)] and the surface modes exhibit significant overlap and thus cannot be treated as fully confined to either condensate boundary.

This thin-shell result can be compared with the case of a more general, thicker condensate shell described by the bubble trap of Eq. (4). In this case, the surface modes of the condensate have frequencies given by

$$\omega_{\text{in,out}}^2 = \frac{\omega_0^2 \ell (R^2 - \Delta)}{\sqrt{(\Delta - R^2)^2/4 + \Omega^2}} (2\nu + 1), \quad (26)$$

where the wave number associated with each surface mode is $q_{\text{in,out}} = \ell/R_{\text{in,out}}$. In other words, for the bubble trap, $F_{\text{in}}q_{\text{in}} = F_{\text{out}}q_{\text{out}}$ leads to a degeneracy in the frequency of surface modes at the inner and outer surfaces. This degeneracy implies that for a hollow condensate with two surfaces that are separated by a substantial thickness, even though the inner surface is smaller in area, its stiffness is lower and can support more oscillations per unit distance (since $q_{\text{in}} > q_{\text{out}}$), bringing the frequency of oscillations with ν nodes on the two surfaces into alignment.

In terms of surface modes, we can therefore identify two different regimes for spherically symmetric BECs: the fully filled BEC sphere where only the outer condensate boundary is available for localization of oscillations, and a hollow BEC shell of nontrivial thickness where the oscillations confined to the inner boundary attain the same frequencies as those confined to its outer surface. In the very thin shell limit, these modes overlap, and their radial nodes do not remain well separated. We note that in all of these regimes the form of the collective modes is functionally the same up to factors that explicitly depend on $r_{\text{in,out}}$ thus capturing the effects of two boundaries and finite thickness in the case of hollow condensates. In the following sections, we discuss the way in which these two regimes connect as a filled spherical BEC hollows out and deforms into a thin, hollow shell.

V. COLLECTIVE MODES: EVOLUTION FROM FILLED SPHERE TO THIN SHELL

We next examine the evolution of a fully filled spherical condensate to a hollow, thin shell geometry and its effect on the system's collective modes. In the extreme limits of the filled sphere and thin shell, we have given analytic predictions in Sec. IV above.

In Sec. VA, we show that the collective mode structure progression for breathing modes from the filled sphere to the thin shell limits detailed above is characterized by a distinctive feature—a dip in frequency. The dip occurs at the point in parameter space when the density at the center of the condensate first begins to vanish—at the hollowing transition. We find that at this transition, density deviations for the radial collective modes localize near the hollowing region. We argue that since the condensate density in this region is highly reduced, the stiffness associated with these modes is also lowered at this point, accounting for the reduced collective mode frequencies.

Density distortions in high angular momentum modes are mainly confined to the boundary surface of the condensate. The effect of an emerging surface on the surface mode frequencies is thus dramatic. In Sec. VB, we detail the evolution of the surface mode structure through the hollowing transition and find a distinct rearrangement of the spectrum at the hollowing transition. We argue that with a new surface present any nodes in the transverse (radial) direction can be distributed between the two (inner and outer) boundary surfaces, thus reducing the energetic cost of hosting these nodes and causing sudden changes in the mode frequencies.

In this section, we analyze systems in the bubble trap potential of Eq. (4), beginning with a survey of the evolution of the spherically symmetric mode frequencies and the corresponding distortions in the condensate density, using the Thomas-Fermi approximation in the hydrodynamic approach. We then corroborate and deepen this analysis using the quench numerics approach of Sec. IIIB. We then analyze finite angular modes with $\ell \neq 0$, including surface modes. A more focused analysis is performed in Sec. VI using different trapping potentials to show that the frequency dip and the surface mode redistribution are robust for a variety of spherically symmetric configurations.

A. Evolution of spherically symmetric modes in the bubble trap

We begin our collective mode analyses by solving the hydrodynamic differential problem in a bubble trap geometry in the Thomas-Fermi limit, given by Eq. (10), using a finite-difference method. This calculation is carried out over a range of mean shell radii $\sqrt{\bar{\Delta}} \equiv \sqrt{\Delta}/R$ thus allowing us to obtain frequencies corresponding to the same collective mode at various stages of the evolu-

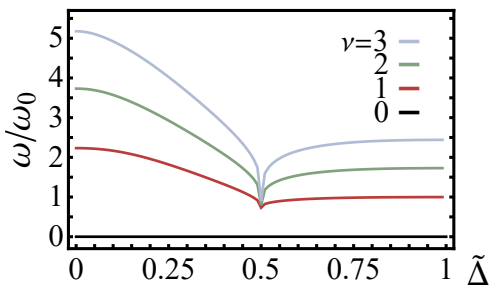


FIG. 3. (Color online) Oscillation frequencies ω , found via the hydrodynamic equation, Eq. (10), with Thomas-Fermi equilibrium profiles, of the three lowest-lying nonzero spherically symmetric ($l = 0$) collective modes $\nu = 1, 2, 3$ (dark red, green, and light blue curves, respectively) vs the bubble-trap detuning $\tilde{\Delta}$ [given $\Delta/\Omega = 1$ in Eq. (4)]. The zero mode (black) is also presented for comparison. As $\tilde{\Delta}$ increases, the BEC evolves from a filled sphere $\tilde{\Delta} = 0$ toward a hollow thin shell $\tilde{\Delta} \rightarrow 1$, through a hollowing transition at $\tilde{\Delta} = 0.5$. In the sphere and thin-shell limits, the frequencies agree with the exact solutions of Eqs. (16) and (20), respectively. Around the transition point, the collective-mode evolution is characterized by a dip in frequency, which is singular in the Thomas-Fermi approximation due to the appearance of a sharp new boundary.

tion between a filled sphere ($\Delta = \tilde{\Delta} = 0$) and a very thin shell ($\Delta \approx R^2$ or $\tilde{\Delta} \approx 1$). We keep the outer edge of the condensate R fixed while the total number of atoms is allowed to vary—this corresponds to working with constant chemical potential μ . This analysis is expected to capture the physics of a condensate in the strong interaction limit.

The Thomas-Fermi density profile gives densities corresponding to a filled sphere at $\tilde{\Delta} = 0$, a filled sphere with depleted central density for $0 < \tilde{\Delta} < 0.5$, and a hollow shell for $0.5 < \tilde{\Delta} < 1$ (the thin-shell limit is $\tilde{\Delta} \rightarrow 1$). The hollow shell has an inner boundary at $R_{\text{in}} = R\sqrt{2\tilde{\Delta} - 1}$, while the filled geometries have no inner boundary. The condition $\tilde{\Delta} = 0.5$ demarcates the sharp transition between the filled and hollow systems. In finite-difference numerics, we section the interval $[0, R]$ ($[R_{\text{in}}, R]$) for the filled (hollow) case into 2^d lattice sites and turn the relevant differential equation into a generalized eigenproblem for a finite-size $(2^d + 1) \times (2^d + 1)$ matrix (see more details in Appendix A). We choose a sufficiently large d that guarantees the convergence of the solution. The data points presented below are for $d = 16$ (unless mentioned otherwise).

In Fig. 3, we plot the oscillation frequencies for the lowest-lying spherically symmetric ($l = 0$) collective modes, including a zero mode and three nonzero modes, as a function of $\tilde{\Delta}$, representing the deformation of the condensate from a filled sphere ($\tilde{\Delta} = 0$) to a thin shell ($\tilde{\Delta} \rightarrow 1$). Note that the zero mode $\nu = 0$, corresponding to a constant density-deviation profile, is not physically detectable for any $\tilde{\Delta}$. We find that the curves do not

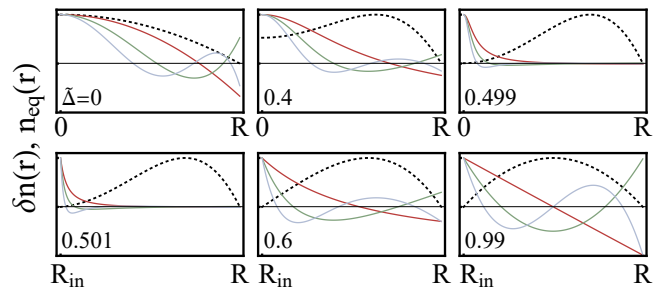


FIG. 4. (Color online) Normalized density deviation profiles $\delta n(r)$ of the three physical breathing modes in Fig. 3 (same convention) and equilibrium profile $n_{\text{eq}}(r)$ (dashed curves). Individual panels correspond to three filled cases $\tilde{\Delta} = 0, 0.4$, and 0.499 , and three hollow cases $0.501, 0.6$, and 0.99 (as labeled inside). Around the hollowing-out transition, the density deviation profiles tend to concentrate on the spherical center. This is energetically favorable and related to the development of frequency dip, as discussed in Sec. VI B.

cross each other and the set of frequencies can distinguish between different stages of the deformation. Frequency values in the two limiting cases are consistent with those predicted for the filled-sphere and thin-shell limits in Eqs. (16) and (20), respectively. There is a frequency dip in each of the three physical modes when the shell develops an inner boundary at $\tilde{\Delta} = 0.5$. The frequencies monotonically decrease (increase) with $\tilde{\Delta}$ if $\tilde{\Delta} < 0.5$ (> 0.5). We have confirmed the stability of this dip structure as the continuum limit is approached (up to $d = 23$). The frequency dip presents a clear signature for the hollowing transition in the system. The physical behavior giving rise to this feature is explored below and in more detail in Sec. VI.

We now turn to the behavior of the density deviations $\delta n(r)$ [recalling that the collective modes of the condensate correspond to $\delta n(\mathbf{r}) = D(r)Y_{\ell m}(\theta, \varphi)$] and their evolution as the system transitions from filled sphere to thin shell. In Fig. 4, we show δn for the lowest three modes and the equilibrium density n_{eq} at six values of $\tilde{\Delta}$. We see that at any stage in the evolution between the sphere and the thin shell, the number of nodes in δn is always equal to the mode index ν , and the maximum amplitude occurs at the center (the inner boundary $r = R_{\text{in}}$) if the center is filled (hollow). When $\tilde{\Delta}$ increases from zero, the central equilibrium density starts to drop. As we approach the hollowing transition at $\tilde{\Delta} = 0.5$, the central density drops to zero and the density deviations attain large amplitudes, localizing at the center of the system. [Note that we still assume a strong interaction such that the linearization of Eq. (7) is valid, i.e., for given scattering length a_s and characteristic interparticle spacing a_d , $a_d\sqrt{a_d/a_s}$ is small compared with the length scale of the concentration.] For $\tilde{\Delta} > 0.5$, i.e., the hollow-shell regime, the density remains zero at R_{in} ($\neq 0$) and the density deviations delocalize from R_{in} as $\tilde{\Delta}$ increases. We recover the Legendre polynomials in the density-deviation pro-

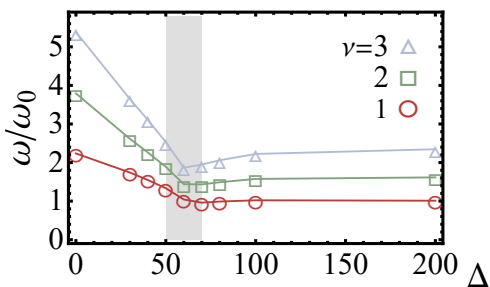


FIG. 5. (Color online) Oscillation frequencies ω , found via the hydrodynamic equation, Eq. (9), with equilibrium profiles given by the numerical solution to the GP equation, of the three lowest-lying nonzero spherically symmetric ($l = 0$) collective modes $\nu = 1, 2, 3$ (circles, squares, and triangles, respectively) vs the bubble-trap detuning Δ . The bubble-trap parameters are set by $\Delta/\Omega = 1$ and the interaction strength is $u = 10^4$. The equilibrium profiles corresponding to five of the data points are shown in Fig. 2. Compared to the Thomas-Fermi results in Fig. 3, the dip in frequency is softened but clearly presents a hollowing transition region (shaded region) between filled and hollow topologies.

files in the thin shell limit of $\tilde{\Delta} = 0.99$, as we have shown in Sec. IV B.

We emphasize the frequency dip at the hollowing transition $\tilde{\Delta} = 0.5$ and the concentration of density deviations around the center as the main results of this section. In assessing the generality of this frequency drop as a signature of a hollow condensate, realistic factors such as moderate interaction strength and nonsharp boundaries need to be taken into account.

As a first step in moving beyond the Thomas-Fermi approximation, we recall that the hydrodynamic formalism for the BEC's dynamical behavior can be applied to any equilibrium density profile, in particular to the numerical ground state of the GP equation. In Fig. 5 we plot the frequencies of the $\nu = 1, 2, 3$ spherically symmetric ($l = 0$) collective modes calculated by using hydrodynamic equation, Eq. (9), with the GP equilibrium density profile found by employing the imaginary-time algorithm. We see that the limiting behavior of the collective mode frequencies is consistent with our discussion in Sec. IV regardless of whether we use the Thomas-Fermi density profile or the more realistic numerical GP result. The dip feature is still present, indicating the development of an inner boundary, but the GP profiles give a less sharp frequency dip compared to the Thomas-Fermi results. In fact, the transition itself spreads across a region, as opposed to a single point. The softened dip feature still reflects the transition region (shaded) between filled and hollow behaviors. The sharpness of the frequency dip is associated with the use of the Thomas-Fermi approximation in which the density profile decreases to zero at condensate edges in an abrupt fashion (as shown in Fig. 2). We will discuss the relevant physics in details in Sec. VI B.

To capture the most general physics beyond both the Thomas-Fermi approximation and the hydrodynamic ap-

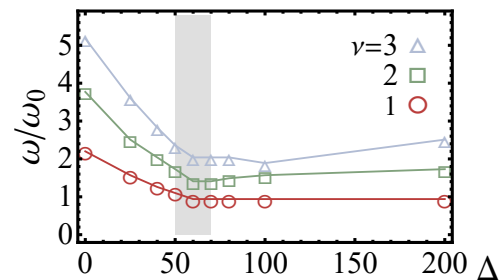


FIG. 6. (Color online) Oscillation frequencies ω , found via quench numerics, of the three lowest-lying nonzero spherically symmetric ($l = 0$) collective modes $\nu = 1, 2, 3$ (same convention as Fig. 5) vs the bubble-trap detuning Δ . The bubble-trap parameters are set by $\Delta/\Omega = 1$ and the interaction strength is $u = 10^4$. In going beyond the Thomas-Fermi approximation of Fig. 5, the singularity in the dip feature around the hollowing transition is softened and spread across the shaded region. However, the drop in frequency from the filled $\Delta = 0$ point and the asymptote to the thin-shell limit for large Δ persists and the spectrum demonstrates that the collective-mode features through the topological transition are robust beyond the hydrodynamic approximation.

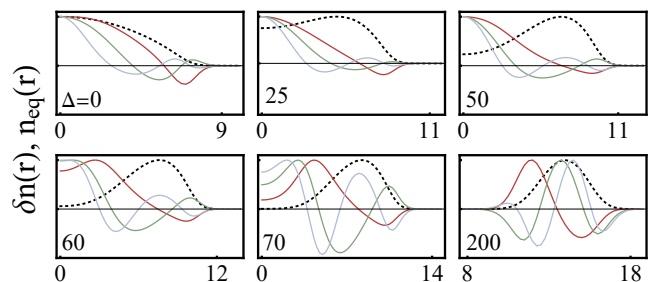


FIG. 7. (Color online) (Color online) Density deviation profiles $\delta n(r)$ of the three breathing modes in Fig. 6 (same convention) and equilibrium profile $n_{\text{eq}}(r)$ (dashed curves). Individual panels correspond to $\Delta = 0, 25, 50, 60, 70$, and 200 (as labeled inside). The radial coordinate (x axis) is presented in the same units as Fig. 2. Similar to the hydrodynamic results in Fig. 4, the density deviation profiles tend to concentrate (but less significantly so) around the spherical center in the hollowing transition region.

proach, we perform sudden quench numerical simulations using the method described in Sec. III B. We simulate BECs throughout their evolution in a bubble-trap from a filled sphere at $\Delta = 0$ to a thin shell at large values of Δ . Figure 6 shows the measured frequencies of the three lowest lying nonzero spherically symmetric collective modes as a function of Δ ranging from 0 to 200, holding $\Delta/\Omega = 1$ and the total number of particles N fixed.

We note the general agreement of the frequency spectrum found using this method with the hydrodynamic results shown in Figs. 3 and 5. This method also gives a more rounded dip feature than that obtained using the Thomas-Fermi approximation. This further supports the

idea that the sharpness of the frequency dip is related to the suddenness with which the sphere hollows as a function of Δ . We observe that the frequency of the $\nu = 1$ mode (shown in red) shows behavior very similar to the results of the hydrodynamic approach with the numerical ground state. As also found with the hydrodynamic approach applied to the numerical ground state, the frequencies of the three modes are well separated when the sphere hollows out, i.e., at the value of Δ where the frequency dips.

Figure 7 shows the deviations of condensate density from equilibrium in the numerical time evolution after a quench for values of Δ that results in the deformation from the filled sphere to the thin shell. We note these density deviations generally reflect those found from the hydrodynamic approach in the Thomas-Fermi approximation (Fig. 4), in that they also show localization of the oscillations to the inner boundary for $\Delta \approx 60$ where the frequency dip occurs as the center of the system becomes hollow.

Arguably these numerical results are more representative of true physical behavior of an experimental system than those obtained using the hydrodynamic approach, which involves a number of previously noted assumptions. The similarity between the two results, especially prominent for hollow shells, justifies the use of the more numerically efficient Thomas-Fermi hydrodynamic approximation. Most importantly, it corroborates our prediction that the dip in the frequency at the values of Δ where the system transitions between the filled sphere and hollow shell is a physical feature that could be observed in an experimental setting.

B. Evolution of modes having $\ell \neq 0$ in the bubble trap

We now examine how collective modes having $\ell \neq 0$ evolve as the condensate is hollowed. We first note that in the eigenvalue problem of Eq. (9) or (10), the nonzero ℓ brings in the term $[V(R) - V(r)]\ell(\ell + 1)/r^2 \propto n_{\text{eq}}(r)\ell(\ell + 1)/r^2$, often called a “centrifugal” term because of its relationship with the angular momentum of the system. Without this term ($\ell = 0$), the right-hand side (RHS) of Eq. (10) has only r -derivative terms, which naturally guarantee a (unphysical) zero-frequency mode $\nu = 0$ having a uniform density-deviation profile. We will see below that this mode shifts to a finite frequency and hence becomes a physical solution as the centrifugal term contributes for any nonzero ℓ . In addition, if ℓ is large enough such that the centrifugal term dominates over the derivative terms, we shall expect that the low-frequency modes are strongly affected by the potential minima, which correspond to the boundary of the condensate (where $n_{\text{eq}} = 0$). In this case, a filled condensate with only an outer boundary is quite different from a hollow condensate with both inner and outer boundaries, so the high- ℓ collective modes can drastically change when

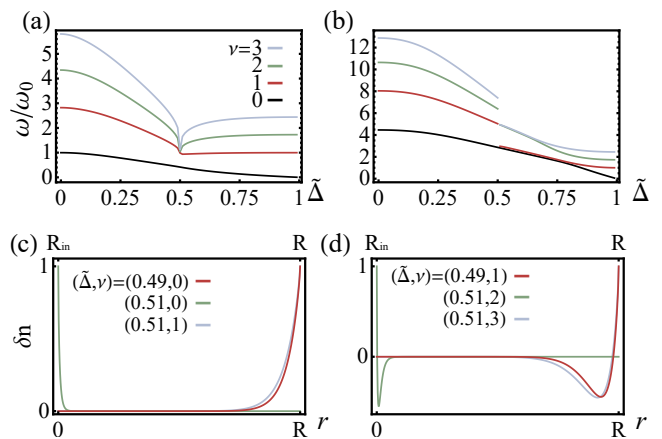


FIG. 8. (Color online) (a) [(b)] Oscillation frequencies ω vs $\tilde{\Delta}$ for $\ell = 1$ ($\ell = 20$) and $\nu = 0, 1, 2, 3$ (same convention as Fig. 3). The $\ell = 1$ (low- ℓ) modes exhibit similar features, including the dip across the hollowing transition $\tilde{\Delta} = 0.5$, as the $\ell = 0$ modes in Fig. 3, except that the $\nu = 0$ mode here has nonzero frequency. The $\ell = 20$ (high- ℓ) modes exhibit sudden drops at the transition. (c) Density deviation profiles δn corresponding to one mode $(\tilde{\Delta}, \nu) = (0.49, 0)$ (dark red) right before the hollowing (axis on bottom), and two modes $(0.51, 0)$ (green) and $(0.51, 1)$ (light blue) right after it (axis on top) in panel (b). (d) Same convention as panel (c) except for modes $(0.49, 1)$ right before the hollowing and $(0.51, 2)$ and $(0.51, 3)$ right after it. Panels (c) and (d) confirm that the high- ℓ modes are surface modes—with density deviation localizing around the condensate surfaces. Before the hollowing ($\tilde{\Delta} = 0.49$), the density deviations of all modes localize around the only surface $r = R$, while after the hollowing ($\tilde{\Delta} = 0.51$), half of them remain around the outer surface $r = R$ and the other half redistribute around the emerging inner surface $r = R_{\text{in}} \approx 0$.

the bubble-trap system starts to hollow out.

We first study the $\ell = 1$ case. Figure 8(a) shows the $\nu \leq 3$ modes obtained from the hydrodynamic approach using Thomas-Fermi equilibrium profiles. We see that the $\nu = 0$ mode now has a finite (and hence physically detectable) frequency that is of the order $O(\omega_{\text{sh}})$ on the filled-sphere side and almost zero in the thin-shell limit, in agreement with the limiting cases studied in Secs. IV A and IV B. The monotonically decreasing curve also shows how these two different energy scales continuously connect through the deformation. The three $\nu > 0$ modes exhibit qualitative features and dip structures similar to those of the $\ell = 0$ case, except the filled-sphere frequencies in the $\ell = 1$ case increase by $O(\omega_{\text{sh}})$ due to the angular oscillation.

We next study a large- ℓ case where the centrifugal term dominates. Figure 8(b) shows the same $\nu \leq 3$ modes for $\ell = 20$. We see that the $\nu = 0$ curve still continuously decreases to zero as we proceed from the filled sphere to the thin shell. For the $\nu > 0$ modes, the dip structure disappears, and the curves exhibit a sudden drop upon the hollowing transition $\tilde{\Delta} = 0.5$. The $\nu = 1$ mode makes

a drop to become nearly degenerate with the $\nu = 0$ mode, and the $\nu = 2$ and $\nu = 3$ modes become equal and continue the evolution of the $\nu = 1$ mode before the drop. In fact, the ν th mode right before the hollowing point and the (2ν) th and $(2\nu + 1)$ th modes right after it are nearly degenerate such that the ν th-mode frequency curve appears to split into two upon the hollowing transition.

We further investigate this splitting in the high- ℓ spectrum by comparing the radial density-deviation profiles $\delta n(r)$ of three nearly degenerate modes—one just before the hollowing ($\tilde{\Delta} = 0.49$) and two just after the hollowing ($\tilde{\Delta} = 0.51$). In Fig. 8(c) [Fig. 8(d)], we plot the density deviation profiles for six specific modes in Fig. 8(b). We see that before the hollowing transition, the modes concentrate near the outer boundary. After hollowing one of the nearly degenerate pair modes localizes near the outer boundary while the other does near the newly created inner boundary. This indicates that the inner minimum of the centrifugal term provides a hollow condensate with additional degrees of freedom for accommodating its collective modes. As the shell becomes thinner, the pair of nearly degenerate modes further split due to a coupling between them through the r -derivative terms in Eq. (10).

Our findings show (i) how the frequencies of pure angular modes ($\nu = 0$, $\ell \neq 0$) of a spherical condensate decrease during the evolution to a shell condensate and (ii) how the high angular modes qualitatively change when the inner boundary is created. These results may find applications in nondestructive measurements for determining the interior structure of a condensate. We will further investigate the relation between the high angular modes and the surface modes in Sec. VIC.

VI. PHYSICS OF THE HOLLOWING-OUT SIGNATURES

In this section, we use our generalized radially shifted trapping potential in order to study the signatures of the hollowing transition over a family of spherically symmetric geometries. These geometries have differing rate of decrease of the condensate equilibrium density near the hollowing center. We provide physical interpretations for the universal signatures of the hollowing transition as well as for the distinct features that arise from specific hollowing-out conditions. (i) We conclude that the sharpness of the nonmonotonic spectral features, namely, the dip at the hollowing transition depends on the rate of central condensate density decay. As a result, the experimentally observed spectrum should still exhibit a universal dip upon the transition. However, the dip is less sharp than the predictions using Thomas-Fermi approximation due to the more realistic equilibrium density distribution with continuous “tails” at the boundaries. (ii) Additionally, while the sudden drop of the surface-mode spectrum is a universal signature due to the emergence of any additional surface upon the hollowing transition, the double degeneracy between inner and outer surface modes of a

hollow shell only occurs for specific geometries, including that of the bubble-trap confinement.

In Sec. VIA, we discuss the general radially shifted potential given in Eq. (5) having two parameters: γ , which tunes the BEC geometry from filled sphere to hollow shell, and α , which controls the decay of the equilibrium density near the center of the system as it hollows. In Sec. VIB, by varying the behavior of the central density, we show that the radial collective mode spectrum exhibits a universal dip at the hollowing transition, but that the sharpness of the dip depends on α . We also use an energetic argument followed by a variational calculation to further understand the frequency dip and the associated concentration of density deviations near the hollowing center. In Sec. VIC, we show that while the hollowing transition always leads to additional surface modes on the inner surface, the mode frequencies depend on the surface stiffness, which in turn depends on α . The frequency degeneracy of the inner and outer surface modes, which we have observed in the bubble trap, corresponds to a special case where $\alpha = 2$. In Sec. VID, we study the hollowing-out physics in a 2D system and show that the collective-mode features are dimension independent.

A. General radially shifted potential

Here we consider the potential given in Eq. (5):

$$V_{\text{gt}}(r) = \frac{1}{2}m\omega_{\text{gt}}^2 R^2 S_l^2 \left[\left(\frac{r}{R} \right)^\alpha - \gamma \right]^2,$$

where γ is a dimensionless parameter that tunes the condensate between sphere and shell geometries, α tunes the condensate equilibrium density profile near the hollowing center, and R specifies a characteristic size.

To understand the geometry of a condensate subject to this trap, we focus on the Thomas-Fermi density profile,

$$n_{\text{eq}}^{\text{gt}}(\mathbf{r}) = n_0^{\text{gt}} \left[1 - \left(\frac{r}{R} \right)^\alpha \right] \left[\left(\frac{r}{R} \right)^\alpha - (2\gamma - 1) \right], \quad (27)$$

with an overall magnitude $n_0^{\text{gt}} = m(\omega_{\text{t}}^{\text{gt}})^2 S_l^2 R^2 / (2U)$. The condensate has its outer boundary at $r = R$ (where $n_{\text{eq}}^{\text{gt}}$ vanishes) and its density maximum at $r = \gamma^{1/\alpha} R \equiv r_0^{\text{gt}}$. This density profile shows that the general trap produces a filled sphere condensate for $\gamma = 0$, a thin-shell condensate for $\gamma \rightarrow 1$, and transitions between them as γ is varied.

At $\gamma = 0$, the condensate forms a fully filled sphere with density $n_{\text{eq}}^{\text{gt}} \propto 1 - (r/R)^{2\alpha}$, exhibiting monotonically decreasing density as one moves radially out from the origin. As γ starts to increase from zero, the maximum density position shifts to a finite radius. For $0 < \gamma < 0.5$, the condensate density at the origin, $n_{\text{eq}}^{\text{gt}}(0) = n_0^{\text{gt}}(1 - 2\gamma)$, remains finite and a local minimum. At $\gamma = 0.5$, the condensate density at the origin becomes zero, signaling the transition from filled to hollow geometry. For $\gamma > 0.5$, we have a hollow shell system with an inner boundary

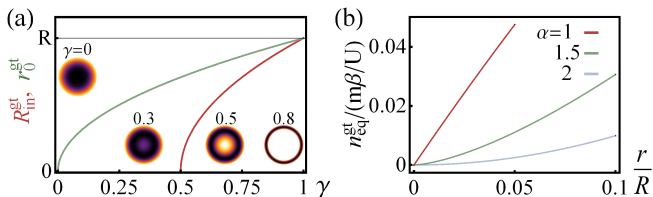


FIG. 9. (Color online) (a) Thomas-Fermi inner boundary $R_{\text{in}}^{\text{gt}}$ (dark red) and maximum-density position r_0^{gt} (green) vs γ for a condensate in the general trap, given by Eq. (5) for $\alpha = 2$. Insets from left to right: schematic density profiles of the condensate at $\gamma = 0, 0.3, 0.5$, and 0.8 , respectively. (b) Thomas-Fermi density profiles $n_{\text{eq}}^{\text{gt}}(r)$ around the center for $\alpha = 1$ (dark red), 1.5 (green), and 2 (light blue) at the hollowing transition $\gamma = 0.5$.

at $R_{\text{in}}^{\text{gt}} = (2\gamma - 1)^{1/\alpha}R$. As $\gamma \rightarrow 1$, the condensate approaches the thin-shell limit, where $V^{\text{gt}}(\mathbf{r})$ can be approximated by the thin-shell potential of Eq. (3) having parameter values $r_0 = r_0^{\text{gt}}$ and $\omega_t^{\text{sh}} = \gamma^{1-1/\alpha}\alpha\omega_t^{\text{gt}} \sim \alpha\omega_t^{\text{gt}}$ (and hence $c = 1/[\gamma^{-1/\alpha} - 1] \gg 1$).

In Fig. 9(a), we plot $R_{\text{in}}^{\text{gt}}$ and r_0^{gt} vs γ and schematic density profiles (insets) for $\alpha = 2$ (quartic double-well) case. The curves show the continuous evolution of the condensate peak density and inner boundary, while the schematics show the density at four stages of the evolution: sphere ($\gamma = 0$), thick shell with filled center (0.3), thick shell at the hollowing transition (0.5), and thin shell (0.8). The variable α determines the power law of the equilibrium profile's growth at the center of the system as $n_{\text{eq}}^{\text{gt}} \propto r^\alpha$. In Fig. 9(b), we plot the Thomas-Fermi profiles near the center of the system at the hollowing transition ($\gamma = 0.5$) for various α . For the bubble-trap potential, the Thomas-Fermi density corresponds to $\alpha = 2$, while the numerical GP solution behaves as $\alpha < 2$ since the condensate wave function has a continuous ‘‘tail’’ at its boundaries.

In Sec. V, we presented results on the collective mode spectrum for the breathing modes in the Thomas-Fermi approximation and using the numerical ground state density, in the bubble-trap potential. We found some universal features (e.g., a dip in the frequency spectrum), as well as some notable differences (e.g., the sharpness of the dip). We see that analyzing the collective modes in the general potential of Eq. (5) and varying α will allow us to distinguish universal signatures of the hollowing transition from those that depend on the central density profile. In the following two sections, we provide a detailed analysis of the effect of α on the spectra of the radial and surface collective modes. We note that for $\alpha \leq 1$, the density profile has a kink (discontinuity in its derivative) at the center, which leads to divergent kinetic energy density $|\partial_r \psi(0)|^2$ and is hence unphysical. Consequently, below we only consider $\alpha > 1$.

B. Spherically symmetric modes at the hollowing transition

From both the hydrodynamic treatment and the sudden quench numerics, we have observed a dip in the frequency spectrum of radial collective modes when the spherical BEC in bubble trap starts to hollow out at its center. However, the results based on a Thomas-Fermi equilibrium density profile show a sharper dip (as in Fig. 3) than those based on a profile from the GP equation (as in Figs. 5 and 6). In addition, we find that the former have density deviations more localizing near the trap center ($r = 0$) than the latter for values of Δ near the hollowing transition. Because the most significant difference between the Thomas-Fermi and GP equilibrium density profiles lies in the central region at the hollowing transition, and the concentrated density deviations are mainly determined by the equilibrium density near the center [through Eq. (8)], one can hypothesize that the shape of central equilibrium density and the sharpness of the frequency dip are closely related. In this section, we study a convenient model using the general-trap profile of Eq. (27) to verify this relationship and confirm that the GP equilibrium density profile leads to a less sharp frequency dip, which should better characterize results in real experimental systems. We also provide evidence based on energetics points and supported by a variational calculation that the frequency dip is always accompanied by the concentration of density deviations at the hollowing transition.

The shape of the central density of a hollowing condensate can be characterized by a power-law index α , such that $n_{\text{eq}}(r) \propto r^\alpha$. As we have shown in Sec. VIA, the general-trap potential can both tune through the sphere-to-shell evolution and control the index α , thus making it ideal for studying the effects of central density during the hollowing transition. Tuning α at $\gamma = 0.5$, the transition point between filled and hollow topologies, can help theoretically isolate the effects of the central density growth ($\propto r^\alpha$). We comment that for a bubble-trap potential, the central Thomas-Fermi profile varies as r^2 when the system is hollowing out. However, the solution of the GP equation is distinctly different due to relatively smooth ‘‘tail’’ near the center associated with a relatively large kinetic energy contribution in this region, which is ignored in the Thomas-Fermi approximation. Therefore a more realistic description of the frequency dip in a bubble traps can be captured by the density growth of modified profile with $\alpha < 2$ than by the original Thomas-Fermi one.

Figure 10(a) shows the frequency of the lowest nonzero radial collective mode ($\nu = 1, \ell = 0$) as a function of γ at various $\alpha \leq 2$, obtained from the hydrodynamic approach. The frequency dip is clearly identifiable near $\gamma = 0.5$ in all three curves, but its sharpness changes with the growth rate α . More precisely, we see that for $\alpha < 2$, the frequency-dip structure is smoother and the minimum-frequency point shifts slightly to $\gamma > 0.5$. In

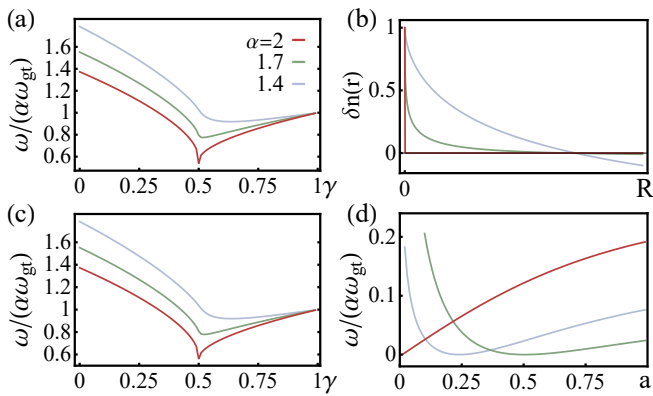


FIG. 10. (Color online) (a) Oscillation frequencies ω for the lowest nonzero breathing mode ($\nu = 1, \ell = 0$) as a function of γ for $\alpha = 2$ (dark red), 1.7 (green), and 1.4 (light blue), obtained by solving the hydrodynamic equation for the general-trap Thomas-Fermi profiles in Eq. (27). (b) The corresponding density deviation profiles δn at the hollowing transition, $\gamma = 0.5$. (c) Oscillation frequencies ω obtained from the variational method. (d) Variational frequency function at $\gamma = 0.5$. Panels (b)–(d) have the same convention as panel (a). Panels (a) and (b) show the dependence of the frequency dip sharpness and the concentration of density deviation profiles on the growth rate of the equilibrium density profile from the hollowing-out center. Panels (c) and (d) show that the dependence originates from the orthonormality and energy minimization of collective mode.

Fig. 10(b), we plot the density deviation profiles $\delta n(r)$ corresponding to each α in Fig. 10(a) at $\gamma = 0.5$. We see that the density deviations become less concentrated at the center as α decreases from 2. As a result, the $\alpha = 2$ density growth, leading to sharp frequency dips and highly concentrated density deviations, agrees with the results for a bubble-trap system with Thomas-Fermi density profiles (as in Figs. 4 and 5). On the other hand, the $\alpha < 2$ density growth, leading to less sharp frequency dip and less concentrated density deviations, agrees with the results using the GP density profiles (as in Figs. 5, 6, and 7). Therefore, the general-trap model captures the main features of the spherically symmetric collective mode frequency spectra during the hollowing transition. We conclude that for a bubble-trap system, using the Thomas-Fermi profile in a general trap and setting $\alpha < 2$ can mimic the more realistic GP profile without the need for numerics.

We next discuss the relationship between the frequency dip and the concentration of density deviations at the hollowing transition. To first provide an energetic argument for interpreting the frequencies of the collective modes, the ν th collective mode has a radial density deviation profile that is orthogonal to all the lower-frequency modes and minimizes the energy (frequency). This is a direct result of the orthonormality of the eigen-solutions of Eq. (8),

$$-\frac{mS_I^2}{U}\omega^2\delta n = \nabla n_{\text{eq}} \cdot \nabla \delta n + n_{\text{eq}} \nabla^2 \delta n.$$

We see from Eq. (8) that the equilibrium density profile contributes to two terms, n_{eq} and ∇n_{eq} . For most of the evolution from a filled sphere to a thin shell, these two terms are not simultaneously zero—we note that at the filled center $\nabla n_{\text{eq}}(0) = 0$ but $n_{\text{eq}}(0) \neq 0$, and at the inner boundary of a fully hollow shell, $n_{\text{eq}}(R_{\text{in}}) = 0$ but $\nabla n_{\text{eq}}(R_{\text{in}}) \neq 0$. At least one of these two terms increases the energy (frequency) and hence disfavors the concentration of density deviations.

However, when the system is at the hollowing transition, both of these terms can become very small in the central region, i.e., the whole differential operator on RHS of Eq. (8) nearly vanishes. In this case, a concentration of density deviation profiles near the center of the system will have a very small energy (frequency) expense and should hence be favored in the low-frequency modes of the system (any density deviation profile spreading away from the center will instead result in a higher frequency). This very small contribution from the RHS of Eq. (8) also leads the mode frequencies to be much lower than those in the filled sphere and the hollow shell (where either n_{eq} or ∇n_{eq} contributes)—hence forming a dip in the frequency spectrum.

We further verify this energetic argument by solving Eq. (9) for the first breathing mode ($\nu = 1, \ell = 0$) by a variational calculation. We consider a variational density deviation profile $D_1(r)$ that has one node ($\nu = 1$) and is orthogonal to the zero mode ($\nu = 0$) with a uniform density deviation D_0 . We then solve for $D_1(r)$ by minimizing the oscillation frequency functional. We adopt a variational ansatz,

$$D_1(r) = \frac{1}{(r/a)^2 + 1} - b. \quad (28)$$

This density deviation profile has a node at $r = a\sqrt{b^{-1} - 1}$. Orthogonality to the zero mode can be guaranteed by choosing b such that $\int D_0 D_1(r) r^2 dr = 0$. With this ansatz, we compute the frequency ω as the expectation value of the differential operator of Eq. (9), namely,

$$\frac{mS_I^2}{U}\omega^2 = \frac{\int n_{\text{eq}}(\partial_r D_1)^2 r^2 dr}{\int D_1^2 r^2 dr}. \quad (29)$$

The solution can then be obtained by minimizing ω with respect to the only free parameter a .

In Fig. 10(c), we plot the variational results for various values of α . We see that the frequency dips upon the hollowing out and that the dependence of dip sharpness on the density profile are identical to those in Fig. 10(a) given by the hydrodynamic equation. In Fig. 10(d), we plot the frequency of this mode at the hollowing transition, $\gamma = 0.5$, as a function of the variational parameter a , which is also the full width at half maximum of the density deviation profile. We see that for the $\alpha = 2$ case (with a sharp dip in the spectrum), $a \rightarrow 0$ directly leads to the minimization of frequency, and that therefore the density deviation will be localized to the center. For the $\alpha < 2$ cases (with a smooth dip), the frequency minimization occurs at nonzero a , giving density deviations with

some small, but nonzero, width. These variational results not only agree with those given the hydrodynamic equation but also corroborate the energetic argument that the density deviations localizing near the hollowing center is directly related to the dip in frequency.

We conclude that independent of the specific shape of the confining trap, any condensate system that transitions between a filled sphere and a hollow shell will display a universal signature of its hollowing. Specifically, radial collective mode spectrum exhibits a frequency minimum at the hollowing transition. This is a rather remarkable result since it allows one to deduce the appearance of a hollowing region deep within the condensate by imaging lowest-lying collective excitations of the system, which can be observed on even the outer surface, possibly even nondestructively.

C. Surface modes at the hollowing transition

We now turn to large- ℓ collective modes, which manifest themselves as distortions localized near the boundary as the condensate's surface modes [66]. The localization of these modes is due to the dominant centrifugal term $\ell(\ell + 1)n_{\text{eq}}$ in Eq. (9), which becomes small only near the boundary, where $n_{\text{eq}} = 0$. For our hollowing system, the significant feature is that a hollow spherical shell supports similar minima in this term on both its inner and outer surfaces. When the system becomes hollow, the creation of the new inner boundary enables the localization of large- ℓ density deviations to the inner surface. The availability of the emerging surface doubles the surface mode spectrum such that half of modes remain at the outer surface but the other half redistribute to the inner surface.

The surface mode frequencies are determined by the properties of the surfaces, as discussed in Sec. IV C and seen specifically in Eq. (15). Focussing on the general-trap potential in the shell region, $\gamma \geq 0.5$, we linearize the trapping potential and the corresponding Thomas-Fermi equilibrium density close to the inner and outer boundaries, R_{in} and $R_{\text{out}} = R$, respectively, in order to find

$$n_{\text{eq}}^{\text{TF}}(x_{\text{in,out}}) = -\frac{F_{\text{in,out}}}{U}x_{\text{in,out}}, \quad (30)$$

with $F_{\text{in,out}} = -\nabla V_{\text{gt}}(R_{\text{in,out}})$ and $x_{\text{in,out}} \leq 0$ the local variable pointing along the direction of $F_{\text{in,out}}$. Employing the equilibrium density profile of Eq. (27) to leading order in $|r - R_{\text{in,out}}|$ in the hydrodynamic equation of motion, Eq. (13) yields the wave number associated with each surface mode given by $q_{\text{in,out}} = \ell/R_{\text{in,out}}$ and

$$\begin{aligned} \omega_{\text{out}}^2 &= \alpha\omega_{\text{gt}}^2 S_l^2 \ell(1-\gamma)(2\nu_{\text{in,out}} + 1), \\ \omega_{\text{in}}^2 &= \alpha\omega_{\text{gt}}^2 S_l^2 \ell(2\gamma - 1)^{1-2/\alpha}(1-\gamma)(2\nu_{\text{in,out}} + 1). \end{aligned} \quad (31)$$

As before, indices ν_{in} and ν_{out} in these expressions count the nodes of radial oscillations confined to the inner or the

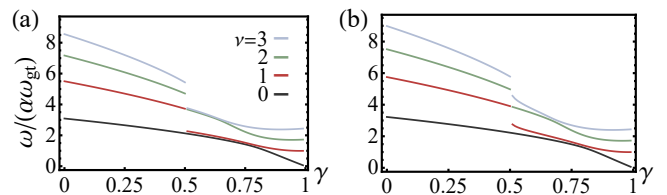


FIG. 11. (Color online) (a) [(b)] Oscillation frequencies ω of high-angular-momentum modes $\ell = 20$ in the general-trap case vs γ for $\nu = 0, 1, 2, 3$ (same convention as Fig. 3) and $\alpha = 2$ (1.85). Comparing (a) and (b), we see that the sudden drop of surface-mode frequency is a universal feature for the hollowing transition, but the degeneracy between outer and inner surface modes of hollow condensates only occurs at $\alpha = 2$.

outer boundary surface, respectively (rather than counting the total number of radial nodes $\nu_{\text{in}} + \nu_{\text{out}}$ across the entire shell which is denoted by ν).

We note that for the $\alpha = 2$ case [including the bubble-trap one in Fig. 8(b)], there is a degeneracy in the frequency of surface modes at the inner and outer surfaces: $\omega_{\text{in}}^2 = \omega_{\text{out}}^2$. If $\alpha \neq 2$, this double degeneracy no longer exists, but the frequency spectrum still exhibits a clear drop due to the mode redistribution to the newly emerging inner surface. In Fig. 11(a) [Fig. 11(b)], we plot the oscillation frequency spectrum of the high-angular-momentum mode $\ell = 20$ for the general-trap case with $\alpha = 2$ (1.85). We see that near the hollowing-out region $\gamma \gtrsim 0.5$, the double degeneracy occurs at $\alpha = 2$ but no longer exists at $\alpha = 1.85$, in agreement with the surface-mode characteristics in Eq. (31). In the thin-shell region $\gamma \lesssim 1$, the modes strongly couple with each other and are no longer degenerate (neither localize near the surface anymore). The restructuring of the large- ℓ surface mode spectrum is a direct and universal signature of a newly emerging surface and hence the hollowing transition.

D. The hollowing transition in two dimensions

Here, we investigate whether the hollowing-out physics we have found for a 3D spherical system also occurs in an analogous 2D geometry. We obtain the collective-mode frequency spectra of a condensate in a 2D bubble trap, which realizes the hollowing transition from a filled disk to a hollow ring. The trap takes the same form as the 3D bubble trap of Eq. (4) except the coordinates are restricted to the x - y plane ($z = 0$). The 2D density deviation profile for a circularly symmetric condensate has the form $\delta n(\mathbf{r}) = D(r)e^{i\ell\phi}$. Employing this form in hydrodynamical equation of Eq. (8) yields the differential eigen equation,

$$\frac{mS_l^2}{U}\omega^2 r D = -\frac{d}{dr} \left(r n_{\text{eq}} \frac{dD}{dr} \right) + \frac{\ell^2 n_{\text{eq}}}{r} D. \quad (32)$$

In Fig. 12, we show the 2D collective-mode spectrum for the Thomas-Fermi equilibrium density profile n_{eq} ,

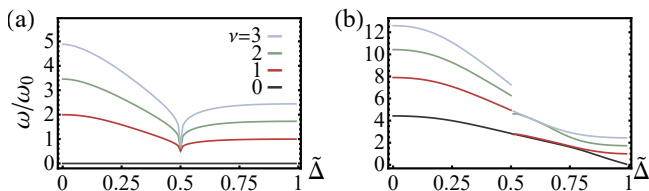


FIG. 12. (Color online)(a) [(b)] Oscillation frequencies ω of a 2D condensate vs 2D bubble-trap parameter $\tilde{\Delta}$ for breathing modes $\ell = 0$ (edge modes $\ell = 20$) and $\nu = 0, 1, 2, 3$ (same convention as Fig. 3). Both panels show the same collective-mode features in the filled-to-hollow evolution and upon the hollowing transition as in 3D cases, indicating that the hollowing-out physics is dimension independent.

which exhibits a sharp hollowing transition at $\tilde{\Delta} = 0.5$ (just as in the 3D case). Panel (a) shows that the breathing mode ($\ell = 0$) frequencies are nonmonotonic with $\tilde{\Delta}$ and develop a sharp dip at the 2D hollowing transition. A variational analysis confirms that the frequency dip in this 2D system can be derived from the orthonormality and energy minimization of the collective modes and is associated with the density deviation concentrating in the central hollowing region. Figure 12(b) shows that the high- ℓ ($\ell = 20$) mode frequencies exhibit a sudden drop at the transition. Examining the density deviation profiles, we find that the high- ℓ modes are edge modes, analogous to the surface modes in the 3D case. The frequency drop of these edge modes at the hollowing transition results from the redistribution of half of the radial nodes to the emerging inner edge of the ring. Performing a similar analysis for the edge modes in this disk geometry as we did for the surface modes in the spherical geometry, we confirm that the degeneracy of outer and inner edge modes in the hollow region is due to the quadratic growth rate of the equilibrium density profile from the center, a specific property of the bubble trap.

In summary, by considering a radially symmetric system in two dimensions, we see that signatures of the hollowing transition exhibited by the collective-mode spectrum are the same in both three and two dimensions. This indicates that the signatures are due to the physics of central hollowing, rather than details of geometry or dimension. We remark that both disk-shaped and ring-shaped BECs have been well studied theoretically [68, 69] and experimentally [12, 13]. The transition regime between these 2D topologies is potentially achievable but has not been studied, to our knowledge. Our findings not only detail the collective-mode physics in the transition regime but also reveal universal features in hollowing-out condensate systems.

VII. EFFECTS OF GRAVITY

So far we have examined the equilibrium profiles and dynamical behavior of spherically symmetric BECs as

their spatial topology is changed from filled to hollow. We now discuss gravitational effects which cannot be neglected in experimental shell traps on Earth. Crucially, unlike in a harmonically trapped system, in a shell-shaped trapped system the gravitational force tends to cause sag: mass accumulation at the lower vertical points in the system and a depletion around the highest. This gravitational sag has been experimentally shown to produce quasi-2D systems having no closed shell-like surfaces under ordinary gravitational conditions on Earth. We estimate the gravitational strength at which the density of the top region of the condensate becomes completely depleted for a thin-shell geometry within the Thomas-Fermi approximation and arrive at a precise value for the critical number of atoms to produce a closed thin-shell structure. Finally, in a perturbative treatment, we analyze the effect of low gravity on the collective mode structure of a very thin condensate shell. We find that gravity couples modes with adjacent angular momentum indices. This is consistent with the fact that a condensate shell in a gravitational field is not fully spherically symmetric. Our estimates show that for typical cold atomic experimental settings, microgravity facilities are the most promising for studying the rich collective mode structure of closed condensate shells.

A. Behavior of equilibrium density and open shells

First, we identify the condition for treating gravity as a small effect compared to the strength of interactions between the atoms in the condensate. We work in the strong interaction and thin shell limits of the radially shifted harmonic potential discussed in Sec. IV B. This geometry can be achieved by the bubble trap. In order to arrive at the needed condition, we consider the case in which the effect of gravity shifts the trap minimum by an amount much smaller than the thickness of the BEC shell, as determined by the strength of interatomic interaction. More precisely, as noted in Sec. IV B, the thickness of the condensate shell can be obtained from the Thomas-Fermi density profile after fixing the number of particles, N , as was found in Eq. (18),

$$\delta = \frac{1}{2} \left(\frac{3UN}{m\pi\omega_{\text{sh}}^2 S_l^2 r_0^2} \right)^{1/3}.$$

The displacement of the trap minimum away from its center due to gravity [70] is equal to

$$r_{\text{disp}} = \frac{g}{\omega_{\text{sh}}^2 S_l}. \quad (33)$$

Hence, the influence of gravity is small compared to the strength of interactions in the condensate when

$$r_{\text{disp}} \ll \delta. \quad (34)$$

When this condition is satisfied, we expect the BEC shell to be largely unchanged in shape despite the influence

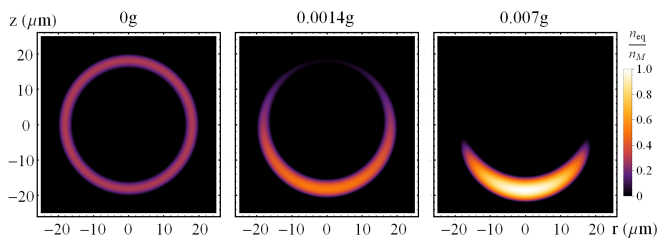


FIG. 13. (Color online) Thomas-Fermi density profiles for condensates confined by the bubble trap without gravity (left) and under the influence of gravitational fields $0.0014g$ (middle) and $0.007g$ (right), where g is the gravitational acceleration on Earth. These profiles are generated for 10^5 ^{87}Rb atoms forming a condensate shell with outer radius $20\ \mu\text{m}$ and thickness $4\ \mu\text{m}$ in the absence of gravity. The colors in the bar graph represent density normalized by $n_M = 3.1 \times 10^{13}/\text{cm}^3$. As the strength of the gravitational field increases, we observe a density depletion at the top of the condensate shell and a density maximum at its bottom.

of gravity. In experimental efforts of Refs. [62, 63], the quantity analogous to Eq. (33) is reported to be comparable to the entire size of the condensate cloud. In this case, the condition for weak gravity is clearly violated and a radical, flattening, deformation of the condensate shell is found by the authors.

As an intermediate stage between these two possibilities—weak gravity that does not change the shape of the condensate shell and very strong gravity that effectively collapses it into a quasi 2D geometry—we consider a set of experimental parameters for which gravity deforms the BEC shell to have most density at its bottom and a heavily depleted top region. This change in condensate density is shown for the bubble trap and multiple values of gravitational field smaller than Earth’s gravity in Fig. 13.

To examine the deformation analytically, we work within the Thomas-Fermi approximation and consider the thin-shell limit of the potential described by Eq. (3) with an added gravitational term. Specifically, adding $-gr \cos \theta$ to the potential and completing the square, we obtain

$$V(r, \theta) = \frac{m\omega_{\text{sh}}^2 S_l^2}{2} \left[(r - r_0) + \frac{g \cos \theta}{\omega_{\text{sh}}^2 S_l} \right]^2 + \left(mgS_l r_0 \cos \theta - \frac{mg^2 \cos^2 \theta}{2\omega_{\text{sh}}^2} \right), \quad (35)$$

where r_0 is the trap minimum in the absence of gravity. For the bubble trap, the frequency of small single-particle oscillations is given by $\omega_{\text{sh}} = \sqrt{\Delta/\Omega\omega_0}$ and the trap minimum is $r_0 = \sqrt{\Delta}$.

The potential in Eq. (35) is equivalent to a radially shifted harmonic trap in the variable $r - r_0$, with the trap minimum vertically displaced away from the center of the condensate shell. This vertical displacement is

equivalent to adding a potential term

$$V_{\text{offset}}(\theta) = mgS_l r_0 \cos \theta - \frac{mg^2 \cos^2 \theta}{2\omega_{\text{sh}}^2}. \quad (36)$$

From the Thomas-Fermi equilibrium density, Eq. (6), we see that the density at the top of the shell vanishes when the chemical potential is equal to $\mu_c = V_{\text{offset}}(\theta = 0)$. This corresponds to the condensate shell “opening up” and can, in extreme cases, lead to the shell approaching a quasi-2D geometry as in Refs. [62, 63].

When the chemical potential attains the critical value μ_c , the inner and the outer radii of the shell are the solutions of $\mu_c - V(r) = 0$. Previously, when the effects of gravity were not taken into account, we typically fixed the outer radius of the condensate as $r = R$, with R being some constant chosen in accordance with experimental data. Once gravity is accounted for, the condensate shell is not perfectly spherically symmetric, so there is no longer a single, θ -independent, outer radius R . Similarly, in the presence of gravity, the thickness of the shell varies with the polar angle as

$$\delta(\theta) = 2r_0 \sqrt{\tilde{g}(1 - \cos \theta)(2 - \tilde{g} - \tilde{g} \cos \theta)}, \quad (37)$$

where we have introduced the dimensionless parameter $\tilde{g} = g/S_l r_0 \omega_{\text{sh}}^2$. We take the condensate shell corresponding to the potential of Eq. (35) to be very thin for $\tilde{g} \ll 1$ and refer to these values of \tilde{g} as the thin shell limit in analogy with our discussion in Sec. IV B.

We note that $\delta(0) = 0$, as expected since we have chosen the chemical potential to cause a density depletion at the top of the condensate shell. Additionally, for $\theta = 0$ we find $r_{\text{max}} = r_{\text{min}} = r_0 - \frac{g}{\omega_{\text{sh}}^2 S_l}$ and since these values should correspond to coordinates on top of the BEC shell we require that

$$r_0 > \frac{g}{\omega_{\text{sh}}^2 S_l}. \quad (38)$$

This is a rather natural constraint given that in the classical problem of an oscillator in a gravitational field, the frequency of oscillation is given by $\omega = \sqrt{g/L}$ for L the size of the object that is oscillating. In other words, the condition in Eq. (38) requires the trapping frequency to be larger than the oscillation frequency naturally associated with gravitational effects. These observations fully characterize the geometry of the condensate shell deformed by gravity.

Furthermore, as is relevant in experimental settings, total particle number conservation requires

$$N_c = 2\pi \int_{r_{\text{min}}}^{r_{\text{max}}} \int_0^\pi n_{\text{eq}}(r, \theta) r^2 \sin \theta dr d\theta, \quad (39)$$

which, evaluated in the thin shell limit, is equivalent to

$$N_c = \frac{128m\pi g^{3/2} r_0^{7/2} S_l^{1/2}}{15U\omega_{\text{sh}}}. \quad (40)$$

Since this expression only includes the gravitational acceleration and trap parameters (the minimum of the harmonic trapping potential r_0 and the frequency of single-particle oscillations around the trap minimum ω_{sh}), it can be used to predict at what particle number the effects of gravity will cause a density depletion at the top of the condensate shell.

Accordingly, given fixed trap parameters, a value of N can be chosen in such a way that the thin condensate shell keeps an approximately uniform density profile regardless of gravitational effects: Choosing a number of atoms larger than N_c guarantees a smaller deformation of the shape of the BEC shell under the influence of gravity. In the limit of $g \rightarrow 0$ the number of atoms needed in order to form a condensate shell robust to the influence of gravity, N_c , vanishes and it also diminishes as ω_{sh} , the trapping frequency, is increased. In other words, an equivalent of the weak gravity regime can be reached by using tighter confinement for the trapped atoms as well.

Furthermore, Eq. (40) implies that given a fixed number of atoms forming the condensate, a critical value of the gravitational constant g_c can be estimated as

$$g_c = \frac{(15U\omega_{\text{sh}}N)^{2/3}}{(128m\pi)^{2/3}r_0^{7/3}S_l^{1/3}}. \quad (41)$$

In experimental setups where the measured value of g is larger than g_c , the condensate shell is expected to open up on top, rather than maintaining its bubble-like shape, as depicted in Fig. 13. If the effective value of the gravitational constant can be lowered through experimental techniques, or use of special microgravity facilities, we propose that realizing g_{eff} smaller than g_c will result in a robust shell-like geometry of the condensate.

Under experimental conditions within which the value of gravitational acceleration cannot be changed, the expression in Eq. (40) suggests a way in which shell-shaped condensates can also be achieved and maintained without significant gravitational sag. In cases where $N \gg N_c$ is within the range of plausible experimental parameters, gravity can be treated as a small effect on an otherwise stable condensate shell of approximately uniform thickness. We proceed to examine the collective motions of condensate shells under such conditions.

B. Collective modes in presence of gravity

We turn to a discussion of condensate shell dynamics in the presence of gravity. In particular, we consider including gravity in the hydrodynamic formalism. Within this approach, we use the gravitational GP equation and apply the Thomas-Fermi approximation with gravity explicitly accounted for.

We start by considering an addition of the gravitational potential term to Eq. (1) so that $V(\mathbf{r}) = V_{\text{trap}}(r) +$

mgz and consequently obtain

$$\begin{aligned} & \frac{-\hbar^2}{2m}\nabla^2\psi(\mathbf{r},t) + V_{\text{trap}}(r)\psi(\mathbf{r},t) - mgz\psi(\mathbf{r},t) \\ & + U_0|\psi(\mathbf{r},t)|^2\psi(\mathbf{r},t) = i\hbar\partial_t\psi(\mathbf{r},t), \end{aligned} \quad (42)$$

a GP equation with an explicit gravitational term. Further, the corresponding Thomas-Fermi density profile reads

$$n_{\text{eq}}(\mathbf{r}) = \frac{\mu - V_{\text{trap}}(r) - mgz}{U}. \quad (43)$$

The hydrodynamic equations appropriate for a BEC in a nonzero gravitational field are then

$$\begin{aligned} \omega^2\delta n(\mathbf{r}) = & \frac{1}{mS_l^2}\frac{\partial V_{\text{trap}}(r)}{\partial r}\frac{\partial\delta n(\mathbf{r})}{\partial r} + \frac{g}{S_l}\cos\theta\frac{\partial\delta n(\mathbf{r})}{\partial r} \\ & - \frac{g}{rS_l}\sin\theta\frac{\partial\delta n(\mathbf{r})}{\partial\theta} - \left[\frac{\mu - V_{\text{trap}}(r)}{mS_l^2} - \frac{gr}{S_l}\cos\theta\right]\nabla^2\delta n(\mathbf{r}). \end{aligned} \quad (44)$$

This expression, Eq. (44), is the nonzero gravity equivalent of Eq. (8) with the Thomas-Fermi equilibrium density profile, Eq. (43). As in previous sections, we use dimensionless length units rescaled by $S_l = \sqrt{\hbar/(2m\omega)}$.

We proceed to treat the gravitational terms in this equation perturbatively: We assume that the trap parameters have been chosen in accordance with Eq. (40) so that the shape of the shell is largely unchanged by gravitational effects. Additionally, we note that choosing $N \geq N_c$ satisfies the condition in Eq. (34), thus justifying our treatment of the condensate shell thickness as effectively uniform.

As shown in Sec. IV B, for a very thin condensate shell the collective modes are analytically described by

$$\delta n(\mathbf{r}) = \sqrt{\frac{\nu(\nu+1)}{2}}P_\nu\left(\frac{r-r_0}{\delta}\right)Y_{m_\ell}^l(\theta,\phi), \quad (45)$$

where $P_\nu(x)$ are the Legendre polynomials, with the corresponding frequencies given by Eq. (20),

$$\omega_{\nu,\ell}^{\text{sh}} = \omega_{\text{sh}}\sqrt{\nu(\nu+1)}/2.$$

Corrections to these frequencies due to the effects of gravity are then given by the eigenvalues of a matrix with entries equal to

$$\begin{aligned} & \langle\delta n(\mathbf{r})_{\nu,m_\ell}^\ell|V_g(r,\theta)|\delta n(\mathbf{r})_{\nu',m'_\ell}^{\ell'}\rangle = \frac{g}{S_l}\langle\delta n(\mathbf{r})_{\nu,m_\ell}^\ell| \\ & - \frac{1}{r}\sin\theta\frac{\partial}{\partial\theta} + \cos\theta\frac{\partial}{\partial r} + r\cos\theta\nabla^2|\delta n(\mathbf{r})_{\nu',m'_\ell}^{\ell'}\rangle. \end{aligned} \quad (46)$$

In the thin-shell limit, $c \gg 1$, we only consider the matrix elements of Eq. (46) to leading order in c^{-1} , or equivalently, the thickness of the condensate shell, δ . Carrying out this calculation (see more details in Appendix B), we find

$$\begin{aligned} & \langle\delta n(\mathbf{r})_{\nu,m_\ell}^\ell|V_g(r,\theta)|\delta n(\mathbf{r})_{\nu',m'_\ell}^{\ell'}\rangle \approx \frac{g\delta r_0}{S_l}\frac{\nu(\nu+1)}{2\nu+1} \\ & \times [f(\ell,\ell',m_\ell,m_{\ell'})\delta_{\ell,\ell'+1} + g(\ell,\ell',m_\ell,m_{\ell'})\delta_{\ell,\ell'-1}], \end{aligned} \quad (47)$$

where the numerical factors $f(\ell, \ell', m_\ell, m_{\ell'})$ and $g(\ell, \ell', m_\ell, m_{\ell'})$ are given in Appendix B. Noting the Kronecker δ functions in Eq. (47), we conclude that for a fixed ν and ℓ finding the eigenfrequencies and eigenmodes of the system under the influence of gravity is reduced to diagonalizing a matrix with nonzero entries only for

$$\{\nu', \ell', m_{\ell'}\} = \{\nu, \ell \pm 1, m_\ell\}. \quad (48)$$

Consequently, the effect of weak gravity (gravity in the regime where it can be treated perturbatively) on the collective modes of the spherically symmetric thin condensate shell is to mix modes with adjacent angular momentum indices. Therefore, if a collective mode with a fixed number of radial nodes ν and a fixed number of angular modes ℓ is induced under conditions of weak gravity in a thin shell BEC, the number of angular nodes will change while the radial density-deviation profile remains the same. Since the overlap between the collective modes under consideration, Eq. (47) is weighted by both the thickness of the shell and the minimum of the harmonic trapping potential, the mixing effect will be more or less prominent depending on the size of the condensate shell. Further, the same conclusion of gravitationally induced mode mixing can be obtained by making an ansatz $\delta n(r, \theta, \phi) = D(r) \sum_{\ell=0}^{\infty} \sum_{m_\ell=-\ell}^{\ell} C_{\ell m_\ell} Y_{m_\ell}^\ell(\theta, \phi)$, for $C_{\ell m_\ell}$ some appropriate set of constants, and seeking a complete solution to the eigenproblem of Eq. (44).

Finally, we emphasize that Eq. (47) is obtained not only in the weak gravity regime but also the thin shell limit so that the mode mixing effect on a thicker shell would be qualitatively different than on a thin one. To gain insight into the behavior of a thicker shell described by a smaller value of c (larger δ), we note that evaluating the matrix element of Eq. (47) to quadratic order (see Appendix B for more details) in the shell thickness yields terms such as

$$2\delta^2 \begin{pmatrix} \nu & 1 & \nu' \\ 0 & 0 & 0 \end{pmatrix}^2, \quad (49)$$

where we use the Wigner- j symbol. As this symbol is proportional to a Clebsch-Gordan coefficient, we can identify a selection rule for this expression. More precisely, terms of this form vanish unless $\nu' = \nu \pm 1$. Consequently, we posit that away from the thin-shell limit (assuming that gravity can still be treated as weak compared to the strength of interactions between the atoms making up the condensate), gravitational pull leads not only to the mixing of modes with adjacent angular node indices ℓ but also those with adjacent radial node indices ν . The practical impact of the analysis of gravitational effects presented in this section is discussed below.

VIII. APPLICATIONS AND EXPERIMENTAL FEASIBILITY

Having presented an extensive study of spherically symmetric hollow condensates and their behavior in var-

ious limits, we turn to a discussion of experimental feasibility of achieving these configurations. We start by providing a few estimates for experimentally measurable quantities, such as condensate density and collective mode frequency, then turn to the effects of gravity, given its striking influence on shell-shaped BECs on Earth.

As a realistic example, we consider a fully filled spherical ^{87}Rb condensate made up of $N = 10^5$ atoms and created by the potential of Eq. (2) with the bare frequency $\omega = 2\pi \times 500$ Hz and condensate size of $R = 10$ μm . The maximum density of such a system is on the order of 10^{16} cm^{-3} while for a condensate shell of the same size and equivalent confining frequency with $c = r_0/\delta \approx 1000$, we find that the maximum condensate density is on the order of 10^{18} cm^{-3} . Comparing their respective breathing mode frequencies shown in Fig. 3 we find that the $(\nu, \ell) = (1, 0)$ mode in the filled condensate corresponds to $\omega_{1,0}^{\text{sp}} \approx 2\pi \times 1.12$ kHz while the same mode in the thin shell is characterized by $\omega_{1,0}^{\text{sh}} \approx 2\pi \times 0.50$ kHz with the correction given by Eq. (21) on the order of $10^{-6}\%$ and therefore negligible. In other words, recalling our discussing in Sec. V A and Fig. 3, we predict that when the $(\nu, \ell) = (1, 0)$ mode is induced in the fully filled spherical condensate, if the system transitions to a thin shell, its eigenfrequency decreases from $2\pi \times 1.12$ kHz to a value slightly smaller than $2\pi\omega \approx 2\pi \times 0.50$ kHz at the hollowing transition and then increases to reach this value in the very-thin-shell limit. The adiabatic change in the condensate shape from a filled sphere to a very thin, hollow shell therefore results in approximately halving the lowest lying collective mode frequency. Similarly, we calculate $\omega_{2,0}^{\text{sp}} \approx 2\pi \times 1.87$ kHz and $\omega_{2,0}^{\text{sh}} \approx 2\pi \times 0.87$ kHz, a 53% decrease from the fully filled sphere limit to the thin hollow shell geometry. More generally, for all low-lying, $\ell = 0$ modes that are experimentally accessible, we predict the decrease in the collective mode frequency at the hollowing point, compared to the oscillation frequency of the same mode in the fully filled spherical BEC to be rather prominent, on the order of 50% or more. Somewhat higher spherically symmetric modes, such as $\nu = 3$, are good candidates for experimental detection of the further decrease of collective mode frequency at the hollowing point compared to the thin-shell limit as well. The collective mode with $\nu = 3$ shows a 20% change between the hollowing point and the thin-shell limit, which makes it suitable for full observation of the nonmonotonicity of the collective mode frequency spectrum of a hollowing BEC.

Additionally, we note that collective modes with low angular momentum values, such as $\ell = 1$ or $\ell = 2$, exhibit frequency dip features similar to those in frequencies of spherically symmetric $\ell = 0$ modes. In a realistic experimental system that might not have perfect spherical symmetry, such low- ℓ collective modes would be the most likely candidate of study.

Comparing the modes with $\nu = 1$ but different ℓ , we find that $\omega_{1,1}^{\text{sp}} \approx 2\pi \times 1.41$ kHz while $\omega_{1,10}^{\text{sp}} = 2\pi \times 2.96$ kHz and $\omega_{1,20}^{\text{sp}} = 2\pi \times 4.03$ kHz. Identifying large ℓ modes,

such as $\ell = 10$ and $\ell = 20$, with excitations of the condensate localized to a particular boundary surface, we note that these surface modes typically have high oscillation frequencies compared to modes with the same number of radial nodes ν but fewer oscillations in the angular direction. Given our calculations in Sec. IV B, this effect of increasing ℓ is not present in the thin-shell limit since all of the collective modes in this configuration are degenerate with respect to a change in the number of their angular nodes.

For $\ell = 20$, we further examine the drop in collective mode frequency due to the redistribution of surface modes when an inner boundary is available. Noting that collective modes with total number of radial zeros equal to 2ν and $2\nu + 1$ become degenerate immediately after the hollowing out transition takes place, we find that $\omega_{1,20}^{\text{SP}} = 2\pi \times 4.03$ kHz and $\omega_{0,20}^{\text{SP}} = 2\pi \times 2.24$ kHz in the sphere limit drop to $\omega_{1,20}^{\text{sh}} = 2\pi \times 1.50$ kHz. This drop constitutes a decrease on the order of 60% and 30%, respectively. Consequently, we identify the redistribution of surface modes as a rather strong effect on collective mode frequencies.

Finally, repeating our analysis for a thicker shell with $c \approx 20$, we find that the corrections to the collective mode frequencies of the shell due to its nontrivial thickness become approximately 3% of the value obtained while assuming the thin-shell condition $c \rightarrow \infty$ is satisfied. As this is not a very large correction, we conclude that a number of our thin-shell results can potentially be observed in experiments even when creating a very thin condensate shell is not feasible.

We turn now to the effects of gravity in experimentally realistic systems. In contrast to fully filled spherical condensates that are simply shifted by gravity with no effect on their shape, the geometry of a hollow condensate shell is, as we have shown in Sec. VII, rather sensitive to the presence of a gravitational field. Accordingly, experimental parameters such as the trapping frequency, interatomic interaction strength, and the number of atoms in the condensate have to be chosen to satisfy the criteria given by Eq. (40); otherwise, the density of the condensate shell is heavily depleted on its top while the majority of atoms pool at its bottom.

In the presence of ordinary gravity, Eq. (40) constrains the shell radius to be rather small or the trapping frequencies to be rather high. Consequently, a realization of a robust, fully shell-shaped BEC on Earth presents an experimental challenge. We estimate that a thin condensate shell made up of ^{87}Rb atoms confined by a trap with a bare frequency of $2\pi \times 500$ Hz and size on the order of $R \sim 10\mu\text{m}$ would have to be made up of $N_c \sim 10^7$ atoms in order to maintain approximately uniform density and robust shape under the influence of gravity. As current experimental efforts [19, 20] show that even lower bare frequencies are optimal for experiments using an rf-dressed bubble trap, we conclude that the number of atoms needed in order for the condensate shell to maintain its shape despite gravitational sag is impractically

high. In other words, experimental investigations of the behavior and properties of ^{87}Rb BEC shells in Earth's gravity are not feasible and microgravity environments need to be sought. For example, we estimate that for a ^{87}Rb condensate shell composed of 200,000 atoms, as is the case in Ref. [63], of the same size ($R \sim 10\mu\text{m}$) would show significant lack of density on its top and largely consist of a pool of atoms at the trap bottom unless (effective) gravitational acceleration in its environment was smaller than $g_c \sim 0.2$ m/s².

While gravitational sag is often compensated for in experimental studies of ultracold atomic systems on Earth, the shell-shaped geometry makes standard methods such as magnetic levitation or the use of the dipole force challenging. Since the bubble trap employs a dressed-state potential, magnetic levitation is not feasible because the atoms in the condensate are in superpositions of all internal magnetic states. Further, though a dipole force due to a gradient of optical intensity (for instance, achieved by using a far-detuned Gaussian beam) could in principle be used to counteract the effects of gravity, the need for high precision in designing such a gradient makes this approach very difficult. Consequently, we identify microgravity environments, rather than terrestrial setups with gravitational compensation, as an optimal choice for experimentally realizing hollow BEC shells.

In cases where a thin shell can be produced, most likely in microgravity environments such as the ZARM drop tower [64] and the Matter-Wave Interferometry in Microgravity (MAIUS) sounding rocket [71] in Germany, and NASA's Cold Atom Laboratory aboard the International Space Station [22], we also estimate the corrections to the frequencies of the collective modes due to their mixing under the influence of gravity. While the magnitude of these corrections depends on the specific ℓ values of the modes being combined, we generally estimate them to be rather small. In particular for the $\nu = 1, \ell = 1, m_\ell = 0$ mode of a thin ^{87}Rb condensate shell of the size on the order of $1\mu\text{m}$ and a bare frequency of $\omega_0 = 2\pi \times 500$ Hz in microgravity $g \approx 10^{-5}$, we find the fractional correction to the collective mode frequency ω to be $\omega_{\text{grav}}/\omega = 1.00015$. This is a change in the collective mode frequency of approximately 0.015%, which is well below the detection limit in experiments. The magnitude of gravitational mode mixing corrections increases in size with increasing ν , and similarly with increasing ℓ . For instance, for high- ℓ collective modes such as described by $\nu = 1$ and $\ell = 20$ the effect of gravity leads to a 2.5% change in collective mode frequency. As this is still a small correction, we take the strength of gravity rather than the magnitude of ℓ or ν to be the dominant factor for the importance of mode mixing. In other words, the presence or absence of mode-mixing effects in thin, spherically symmetric condensate shells can be interpreted as an indicator of the strength of gravity in experiments where a fully covered shell is realized.

More precisely, we posit that since the change in the frequencies of the collective modes due to mode mixing

is rather small in microgravitational environments, the presence of large frequency corrections due to mode mixing points toward a larger value of gravitational acceleration. For instance, recalling that we estimated that the condensate shell in Ref. [63] would retain its shape for $g_c \approx 0.2 \text{ m/s}^2$ we calculate that the frequency of the $(\nu, \ell) = (1, 0)$ breathing mode in a thin shell of the same size ($R \sim 10 \mu\text{m}$) in a gravitational field determined by g_c would change approximately 27% due to mode mixing. This correction is almost 20,000 times larger than it would be in microgravity. Additionally, a similar mode-mixing behavior would be observed in condensate shells with anisotropy along the z -direction, or clouds closer to a “cigar-shape” rather than a sphere. Therefore, the absence of strong experimental signatures of mode mixing offers a confirmation of both very small values of gravitational acceleration in the environment of the condensate shell and also its full spherical symmetry.

IX. SUMMARY AND CONCLUSION

Our comprehensive study of the collective excitations of hollow BECs offers an understanding of quantum liquids having this unique spatial topology and provides timely predictions for its experimental investigation. A variety of cold atomic trapping potentials are equipped to realize the hollowing transition as a function of a tuning parameter, corresponding to the vanishing of density within the BEC’s interior, the rf-dressed bubble-trap potential being a prime candidate. We have studied density profiles of such BECs by employing appropriate trapping potentials, including a generalized radially shifted potential capable of realizing multiple models of interior density depletion. A realistic description of the central density reduction is especially important for the analysis of the hollowing-out change of the condensate’s real space topology.

We have focused on the collective modes of spherically symmetric BECs and the nonmonotonic features in their frequency spectra that serve as signatures of this topological transition. We have employed a combination of exact analytic and numerical hydrodynamics and real-time GP equation simulations of sudden-quench experiments in a complementary manner. The latter serves as an *in situ* simulation of experimental probe of BEC collective modes thus closely connecting our work to realistic and feasible experimental procedures. We have found that thin shell BECs exhibit quantized collective modes that show a significant frequency splitting due to radial degrees of freedom but are degenerate with respect to angular degrees of freedom. Upon transitioning between filled and hollow topology, the breathing mode frequencies drop to a minimum, and the corresponding density deviations concentrate around the interior point of vanishing density. Additionally, as the hollowing-out occurs, the redistribution of radial nodes in the high-angular-momentum surface modes from the outer to the

emerging inner surface leads to a dramatic drop in their frequency spectrum, constituting strong evidence of the hollowing-out topological transition. We have additionally shown that these nonmonotonic frequency features are robust across a range of trapping potentials. Further, our analysis of the hollowing transition of a 2D disk to a ring indicates that these breathing and surface collective mode spectral signatures are universal for hollowing-out topological transitions.

Finally, we have investigated the effects of gravity on a BEC shell’s ground-state stability and collective-mode frequencies. We have determined critical experimental parameters for achieving condensate shells that are not severely deformed by gravitational sag. For terrestrial experimental conditions, gravity produces a complete density depletion at the top of the shell potential and a pooling of atoms at the bottom of the shell, which leads to a flattening of the 3D shell into a quasi-2D disk. We argue that this sagging effect can be mitigated in microgravity environments, and have made corresponding predictions for the perturbative effects of gravity on the collective mode spectra.

While BECs have already been created in microgravity [64], a series of experiments employing tunable trapping potentials capable of executing a hollowing transition in NASA’s Cold Atom Laboratory (CAL) aboard the International Space Station are expected to be the first experimental realization and investigation of fully closed BEC shells [23]. Our predictions for the collective mode behavior of such shells will be particularly advantageous for probing the hollowing-out phenomena, as direct imaging cannot clearly identify the emergence of an inner surface within a BEC’s interior.

Having exhaustively characterized the behavior of spherically symmetric hollow BECs, many questions concerning similar hollow systems remain to be addressed in the future. For instance, in NASA’s CAL experiments, the effects of asymmetric trapping potentials on the collective modes and the hollowing signatures in, e.g., time-of-flight expansion will be of significant interest. Another major direction concerning hollow shells would entail rotation; resultant vortex formation and distribution in these geometries would exhibit behavior dramatically different from those observed in thin spheres and disk geometries. Our results are also applicable to broader settings of condensate shells in neutron stars, Bose-Fermi mixtures, and Mott-insulator-superfluid coexisting systems; future work would require making concrete connections between these settings and our analyses.

ACKNOWLEDGMENTS

We thank Nathan Lundblad and Ryan Wilson for illuminating discussions. KS acknowledges support by ARO (W911NF-12-1-0334), AFOSR (FA9550-13-1-0045), NSF (PHY-1505496), and Texas Advanced Computing Center (TACC). CL acknowledges support by the National Sci-

ence Foundation under Award No. DMR-1243574. KP, SV, and CL acknowledge support by NASA (SUB JPL 1553869 and 1553885). CL and SV thank the KITP for hospitality.

Appendix A: Finite-difference method

In this section, we present the details for the finite-difference method we use to solve the differential equation for the collective modes. The Sturm–Liouville equation has a general form of

$$[p(x)y']' + q(x)y = -\lambda w(x)y, \quad (\text{A1})$$

where the eigenvalues λ and corresponding eigenfunctions $y(x)$ are to be determined. With a small interval ε , we can approximate the differential term as

$$py'|_x = p(x) \frac{y(x+0.5\varepsilon) - y(x-0.5\varepsilon)}{\varepsilon}, \quad (\text{A2})$$

and hence

$$\begin{aligned} (py')'|_x &= \frac{py'|_{x+0.5\varepsilon} - py'|_{x-0.5\varepsilon}}{\varepsilon} \\ &= \frac{p(x+0.5\varepsilon) \frac{y(x+\varepsilon) - y(x)}{\varepsilon} - p(x-0.5\varepsilon) \frac{y(x) - y(x-\varepsilon)}{\varepsilon}}{\varepsilon} \\ &= \frac{p(x+0.5\varepsilon)y(x+\varepsilon)}{\varepsilon^2} - \frac{[p(x+0.5\varepsilon) + p(x-0.5\varepsilon)]y(x)}{\varepsilon^2} \\ &\quad + \frac{p(x-0.5\varepsilon)y(x-\varepsilon)}{\varepsilon^2}. \end{aligned} \quad (\text{A3})$$

If the domain is sectioned into many lattice sites with lattice spacing ε , a function f can be represented by a vector $\mathbf{f} = \{f_i\}$ such as $f_i = f(x)$ and $f_{i\pm 1} = f(x \pm \varepsilon)$. We then turn Eq. (A3) to

$$(py')'_i = \frac{p_{i+0.5}y_{i+1} - (p_{i+0.5} + p_{i-0.5})y_i + p_{i-0.5}y_{i-1}}{\varepsilon^2}. \quad (\text{A4})$$

Using the rule of Eq. (A4) and treating $q(x)$ and $w(x)$ as diagonal matrices, we can turn Eq. (A1) into a generalized eigen problem for a finite-size matrix. The accuracy can be increased by decreasing ε . By comparing Eq. (A1) with Eq. (10) multiplied by r^2 , we obtain

$$p = r^2 [V(R) - V(r)], \quad (\text{A5})$$

$$q = -l(l+1) [V(R) - V(r)], \quad (\text{A6})$$

$$w = r^2, \quad (\text{A7})$$

$$\lambda = m\omega^2. \quad (\text{A8})$$

Therefore, one can calculate the collective modes by solving the generalized eigen problem for a finite matrix.

Appendix B: Evaluation of matrix elements in the perturbative approach to gravitational hydrodynamic equations

In this section, we present a detailed calculation of the matrix elements of Eq. (46). More precisely, to leading

order in the thickness of the condensate shell, we set out to calculate

$$\begin{aligned} &\langle \delta n(r, \theta, \phi)_{\nu, m}^l | V_g(r, \theta) | \delta n(r, \theta, \phi)_{\nu', m'}^{l'} \rangle \\ &\approx \frac{g}{S_l} \langle \delta n(\mathbf{r})_{\nu, m}^l | -\frac{1}{r} \sin \theta \frac{\partial}{\partial \theta} - \frac{l'(l'+1)}{r} \cos \theta | \delta n(\mathbf{r})_{\nu', m'}^{l'} \rangle. \end{aligned} \quad (\text{B1})$$

To that end, we recall

$$\delta n(r, \theta, \phi)_{\nu, m}^l = \sqrt{\frac{\nu(\nu+1)}{2}} P_\nu \left(\frac{r-r_0}{\delta} \right) Y_{m_\ell}^l(\theta, \phi) \quad (\text{B2})$$

and, further, express the spherical harmonics as

$$Y_m^l(\theta, \phi) = (-1)^m \sqrt{\frac{2l+1}{4\pi} \frac{(l-m)!}{(l+m)!}} P_l^m(\cos \theta) e^{im\phi} \quad (\text{B3})$$

so that the matrix elements we are interested in require evaluating an integral over the polar and azimuthal angles and the radial coordinate. In order to evaluate the first term in Eq. (B1) we start by evaluating the integral over ϕ as

$$\int_0^{2\pi} e^{i(m-m')\phi} d\phi = 2\pi \delta_{m, m'}. \quad (\text{B4})$$

We proceed to utilize the differential identity

$$\begin{aligned} \sin \theta \frac{\partial}{\partial \theta} P_l^m(\cos \theta) &= \frac{1}{2l+1} [l(l-m+1)P_{l+1}^m(\cos \theta) \\ &\quad - (l+1)(l+m)P_{l-1}^m(\cos \theta)] \end{aligned} \quad (\text{B5})$$

and the orthogonality relation

$$\int_{-1}^1 P_k^m(\cos \theta) P_l^m(\cos \theta) \sin \theta d\theta = \frac{2(l+m)!}{(2l+1)(l-m)!} \delta_{k, l} \quad (\text{B6})$$

for the integral over θ . Furthermore, to evaluate the radial integral we carry out a change of variable $x = \frac{r-r_0}{\delta}$ and write

$$\begin{aligned} &\int P_\nu \left(\frac{r-r_0}{\delta} \right) P_{\nu'} \left(\frac{r-r_0}{\delta} \right) r dr \\ &= \delta \int P_\nu(x) P_{\nu'}(x) (\delta x + r_0) dx \end{aligned} \quad (\text{B7})$$

where the factor $\delta x + r_0$ can be expressed as a sum over the Legendre polynomials $P_0(x)$ and $P_1(x)$. More precisely,

$$\delta x + r_0 = \delta P_1(x) + r_0 P_0(x) \quad (\text{B8})$$

so that the integral in Eq. (B7) can be evaluated by recalling that an integral of three Legendre polynomials is proportional to the square of a Wigner- j symbol

$$\int_{-1}^1 P_k(x) P_l(x) P_m(x) dx = 2 \begin{pmatrix} k & l & m \\ 0 & 0 & 0 \end{pmatrix}^2. \quad (\text{B9})$$

The Wigner- j symbol itself is related to a Clebsch-Gordan coefficient

$$C(j_1, j_2, j_3 | m_1, m_2, -m_3) = \langle j_1 m_1, j_2 m_2 | j_3, -m_3 \rangle \quad (\text{B10})$$

by the definition

$$\begin{pmatrix} j_1 & j_2 & j_3 \\ m_1 & m_2 & m_3 \end{pmatrix} = \frac{(-1)^{j_1-j_2-m_3}}{(2j_3+1)^{1/2}} C(j_1, j_2, j_3 | m_1, m_2, -m_3). \quad (\text{B11})$$

We can therefore evaluate the integral in Eq. (B7) as

$$\begin{aligned} & \int P_\nu(x)(\delta x + r_0)P_{\nu'}(x)dx = \\ & \frac{2r_0}{2\nu+1} \delta_{\nu,\nu'} + 2\delta \begin{pmatrix} \nu & 1 & \nu' \\ 0 & 0 & 0 \end{pmatrix}^2 \end{aligned} \quad (\text{B12})$$

Combining Eqs. (B5), (B7), (B8), and (B12), we then obtain, to leading order in c^{-1} ,

$$\begin{aligned} & \langle \delta n(\mathbf{r})_{\nu,m}^l | \frac{g}{rS_l} \sin\theta \frac{\partial}{\partial\theta} | \delta n(\mathbf{r})_{\nu',m'}^{l'} \rangle \approx \\ & \frac{g\delta r_0}{S_l} \frac{\nu(\nu+1)}{2\nu+1} \sqrt{\frac{(l'-m)!(l+m)!}{(2l+1)(2l'+1)(l+m)!(l-m)!}} \\ & \times [(l'+1)(l'+m)\delta_{l,l-1} - l'(l-m+1)\delta_{l,\nu'+1}]. \end{aligned} \quad (\text{B13})$$

We move on to calculate the second term in Eq. (B1). First, we note that the integral over the azimuthal angle is equal to $2\pi\delta_{m,m'}$ as above. We then use the recursive identity

$$xP_m^l(x) = \frac{l-m+1}{2l+1}P_{l+1}^m(x) + \frac{l+m}{2l+1}P_{l-1}^m(x) \quad (\text{B14})$$

in order to evaluate the integral over the polar angle

$$\int P_l^m(\cos\theta)P_m^{l'}(\cos\theta)\cos\theta\sin\theta d\theta \quad (\text{B15})$$

by again using the orthogonality relation of Eq. (B6). We conclude that the total angular contribution to this term reads

$$\begin{aligned} & \int Y_m^{l'*}(\theta, \phi)Y_m^l(\theta, \phi)\cos\theta\sin\theta d\theta d\phi \\ & = -\sqrt{\frac{(l+m)!(l'-m)!}{(2l+1)(2l'+1)(l-m)!(l'+m)!}} \\ & \times [(l'-m+1)\delta_{l,\nu'+1} + (l'+m)\delta_{l,\nu'-1}], \end{aligned} \quad (\text{B16})$$

while the radial contribution is given by Eq. (B12). The total contribution of this term is then equal to

$$\begin{aligned} & \langle \delta n(\mathbf{r})_{\nu,m}^l | \frac{gl'(l'+1)}{rS_l} \cos\theta \frac{\partial}{\partial\theta} | \delta n(\mathbf{r})_{\nu',m'}^{l'} \rangle \approx \\ & \frac{-g\delta r_0}{S_l} \frac{\nu(\nu+1)}{2\nu+1} \sqrt{\frac{(l'-m)!(l+m)!}{(2l+1)(2l'+1)(l-m)!(l'+m)!}} \\ & \times [l'(l'+1)(l'-m+1)\delta_{l,\nu'+1} + l'(l'+1)(l'+1)\delta_{l,\nu'-1}]. \end{aligned} \quad (\text{B17})$$

We conclude that to leading order in c^{-1} , or equivalently the shell thickness δ , the matrix element of Eq. (B1) reads

$$\begin{aligned} & \langle \delta n(\mathbf{r})_{\nu,m}^l | V_g(r, \theta) | \delta n(\mathbf{r})_{\nu',m'}^{l'} \rangle \approx \\ & \frac{g\delta r_0}{S_l} \frac{\nu(\nu+1)}{2\nu+1} \sqrt{\frac{(l'-m)!(l+m)!}{(2l+1)(2l'+1)(l-m)!(l'+m)!}} \times \\ & [l'(l'-m+1)(l'+2)\delta_{l,\nu'+1} + (l'+m)(l'^2-1)\delta_{l,\nu'-1}]. \end{aligned} \quad (\text{B18})$$

-
- [1] F. Dalfovo, S. Giorgini, L. P. Pitaevskii, and S. Stringari, Theory of Bose-Einstein condensation in trapped gases, *Rev. Mod. Phys.* **71**, 463 (1999).
- [2] A. J. Leggett, Bose-Einstein condensation in the alkali gases: Some fundamental concepts, *Rev. Mod. Phys.* **73**, 307 (2001).
- [3] E. A. Cornell and C. E. Wieman, Nobel lecture: Bose-Einstein condensation in a dilute gas: The first 70 years and some recent experiments, *Rev. Mod. Phys.* **74**, 875 (2002).
- [4] W. Ketterle, Nobel lecture: When atoms behave as waves: Bose-Einstein condensation and the atom laser, *Rev. Mod. Phys.* **74**, 1131 (2002).
- [5] C. J. Pethick and H. Smith *Bose-Einstein Condensation in Dilute Gases*, 2nd, ed. (Cambridge University Press, Cambridge, UK, 2008).
- [6] I. Bloch, J. Dalibard, and W. Zwerger, Many-body physics with ultracold gases, *Rev. Mod. Phys.* **80**, 885 (2008).
- [7] A. Gorlitz, J.M. Vogels, A. E Leanhardt, C. Raman, T. L. Gustavson, J. R. Abo-Shaeer, A. P. Chikkatur, S. Gupta, S. Inouye, T. Rosenband, and W. Ketterle, Realization of Bose-Einstein Condensates in Lower Dimensions, *Phys. Rev. Lett.* **87**, 130402 (2001).
- [8] M. Greiner, I. Bloch, O. Mandel, T. W. Hansch, and T. Esslinger, Exploring Phase Coherence in a 2D Lattice of Bose-Einstein Condensates, *Phys. Rev. Lett.* **87**, 160405 (2001).
- [9] S. Dettmer, D. Hellweg, P. Ryytty, J. J. Arlt, W. Ermer, K. Sengstock, D. S. Petrov, G. V. Shlyapnikov, H. Kreutzmann, L. Santos, and M. Lewenstein, Observation of Phase Fluctuations in Elongated Bose-Einstein Condensates, *Phys. Rev. Lett.* **87**, 160406 (2001).
- [10] G. Hechenblaikner, J. M. Krueger, and C. J. Foot, Properties of quasi-two-dimensional Condensates in Highly Anisotropic Traps, *Phys. Rev. A* **71**, 013604 (2005).
- [11] N. L. Smith, W. H. Heathcote, G. Hechenblaikner, E. Nugent, and C. J. Foot, Quasi-2D Confinement of a BEC

- in a Combined Optical and Magnetic Potential, *J. Phys. B* **38**, 223 (2005).
- [12] S. Gupta, K. W. Murch, K. L. Moore, T. P. Purdy, and D. M. Stamper-Kurn, Bose-Einstein Condensation in a Circular Waveguide, *Phys. Rev. Lett.* **95**, 143201 (2005).
- [13] A. Ramanathan, K. C. Wright, S. R. Muniz, M. Zelan, W. T. Hill, III, C. J. Lobb, K. Helmerson, W. D. Phillips, and G. K. Campbell, Superflow in a Toroidal Bose-Einstein Condensate: An Atom Circuit with a Tunable Weak Link, *Phys. Rev. Lett.* **106**, 130401 (2011).
- [14] A. L. Gaunt, T. F. Schmidutz, I. Gotlibovych, R. P. Smith, and Z. Hadzibabic, Bose-Einstein Condensation of Atoms in a Uniform Potential, *Phys. Rev. Lett.* **110**, 200406 (2013).
- [15] A. Smerzi, S. Fantoni, S. Giovanazzi, and S. R. Shenoy, Quantum Coherent Atomic Tunneling between Two Trapped Bose-Einstein Condensates, *Phys. Rev. Lett.* **79**, 4950 (1997).
- [16] Y. Shin, M. Saba, T. A. Pasquini, W. Ketterle, D. E. Pritchard, and A. E. Leanhardt, Atom Interferometry with Bose-Einstein Condensates in a Double-Well Potential, *Phys. Rev. Lett.* **92**, 050405 (2004).
- [17] S. Hofferberth, I. Lesanovsky, B. Fischer, J. Verdu, and J. Schmiedmayer, Radiofrequency-dressed-state Potentials for Neutral Atoms, *Nat. Phys.* **2**, 10, 710 (2006).
- [18] C. Lannert, T.-C. Wei and S. Vishveshwara, Dynamics of condensate shells: Collective modes and expansion, *Phys. Rev. A* **75**, 013611, (2007).
- [19] N. Lundblad (private communication).
- [20] N. Lundblad, T. Jarvis, D. Paseltiner, and C. Lannert, Progress toward studies of bubble-geometry Bose-Einstein condensates in microgravity with a ground-based prototype of NASA CAL, *DAMOP Meeting*, K1.00119 (2016).
- [21] O. Zobay and B. M. Garraway, Two-Dimensional Atom Trapping in Field-Induced Adiabatic Potentials, *Phys. Rev. Lett.* **86**, 1195 (2001); Atom trapping and two-dimensional Bose-Einstein condensates in field-induced adiabatic potentials, *Phys. Rev. A* **69**, 023605 (2004). <http://coldatomlab.jpl.nasa.gov>
- [22] E. Gibney, Universe's coolest laboratory set to open up quantum world, *Nature (London)* **557**, 151 (2018).
- [24] J. M. Kosterlitz and D. J. Thouless, Ordering, metastability and phase transitions in two-dimensional systems, *J. Phys. C: Solid State Phys.* **6** 1181 (1973).
- [25] D. Jaksch, C. Bruder, J. I. Cirac, C. W. Gardiner, and P. Zoller, Cold Bosonic Atoms in Optical Lattices, *Phys. Rev. Lett.* **81**, 3108 (1998).
- [26] D. van Oosten, P. van der Straten, and H. T. C. Stoof, Quantum phases in an optical lattice, *Phys. Rev. A* **63**, 053601 (2001).
- [27] M. Greiner, O. Mandel, T. Esslinger, T. W. Hansch, and I. Bloch, Quantum phase transition from a superfluid to a Mott insulator in a gas of ultracold atoms, *Nature (London)* **415**, 39 (2002).
- [28] M. Greiner, Ultracold quantum gases in three-dimensional optical lattice potentials, Ph.D. thesis, Ludwig-Maximilians-Universität at München, Germany, 2003.
- [29] M. P. A. Fisher, P. B. Weichman, G. Grinstein, and D. S. Fisher, Boson localization and the superfluid-insulator transition, *Phys. Rev. B* **40**, 546 (1989).
- [30] K. Sheshadri, H. R. Krishnamurthy, R. Pandit, and T. V. Ramakrishnan, Superfluid and insulating phases in an interacting-boson model: Mean-field theory and the RPA, *EPL* **22**, 257 (1993).
- [31] J. K. Freericks and H. Monien, Phase diagram of the Bose-Hubbard Model, *EPL* **26**, 545 (1994).
- [32] G. Batrouni, V. Rousseau, R. Scalettar, M. Rigol, A. Muramatsu, P. Denteneer, and M. Troyer, Mott Domains of Bosons Confined on Optical Lattices, *Phys. Rev. Lett.* **89** 117203 (2002).
- [33] B. DeMarco, C. Lannert, S. Vishveshwara, and T.-C. Wei, Structure and stability of Mott-insulator shells of bosons trapped in an optical lattice, *Phys. Rev. A* **71**, 063601 (2005).
- [34] G. K. Campbell, J. Mun, M. Boyd, P. Medley, A. E. Leanhardt, L. G. Marcassa, D. E. Pritchard, and W. Ketterle, Imaging the Mott Insulator Shells by Using Atomic Clock Shifts, *Science* **313**, 649 (2006).
- [35] R. A. Barankov, C. Lannert, and S. Vishveshwara, Coexistence of superfluid and Mott phases of lattice bosons, *Phys. Rev. A* **75**, 063622 (2007).
- [36] K. Sun, C. Lannert, and S. Vishveshwara, Probing condensate order in deep optical lattices, *Phys. Rev. A* **79**, 043422 (2009).
- [37] K. Mølmer, Bose Condensates and Fermi Gases at Zero Temperature, *Phys. Rev. Lett.* **80**, 1804 (1998).
- [38] S. Ospelkaus, C. Ospelkaus, L. Humbert, K. Sengstock, and K. Bongs, Tuning of Heteronuclear Interactions in a Degenerate Fermi-Bose Mixture, *Phys. Rev. Lett.* **97**, 120403 (2006).
- [39] B. V. Schaeybroeck and A. Lazarides, Trapped phase-segregated Bose-Fermi mixtures and their collective excitations, *Phys. Rev. A* **79**, 033618 (2009).
- [40] F. Weber, Strange quark matter and compact stars, *Prog. Part. Nucl. Phys.* **54**, 193 (2004).
- [41] C. J. Pethick, T. Schaefer, and A. Schwenk, Bose-Einstein condensates in neutron stars, [arXiv:1507.05839](https://arxiv.org/abs/1507.05839).
- [42] K. Padavić, K. Sun, C. Lannert, and S. Vishveshwara, Physics of hollow Bose-Einstein condensates, *EPL* **120**, 20004 (2017).
- [43] D. S. Jin, J. R. Ensher, M. R. Matthews, C. E. Wieman, and E. A. Cornell, Collective Excitations of a Bose-Einstein Condensate in a Dilute Gas, *Phys. Rev. Lett.* **77**, 420 (1996).
- [44] M.-O. Mewes, M. R. Andrews, N. J. van Druten, D. M. Kurn, D. S. Durfee, C. G. Townsend, and W. Ketterle, Collective Excitations of a Bose-Einstein Condensate in a Magnetic Trap, *Phys. Rev. Lett.* **77**, 988 (1996).
- [45] M. Edwards, P. A. Ruprecht, K. Burnett, R. J. Dodd, and C. W. Clark, Collective Excitations of Atomic Bose-Einstein Condensates, *Phys. Rev. Lett.* **77**, 1671 (1996).
- [46] S. Stringari, Collective Excitations of a Trapped Bose-Condensed Gas, *Phys. Rev. Lett.* **77**, 2360 (1996).
- [47] Y. Castin and R. Dum, Bose-Einstein Condensates in Time Dependent Traps, *Phys. Rev. Lett.* **77**, 5315 (1996).
- [48] D. M. Stamper-Kurn, H.-J. Miesner, S. Inouye, M. R. Andrews, and W. Ketterle, Collisionless and Hydrodynamic Excitations of a Bose-Einstein Condensate, *Phys. Rev. Lett.* **81**, 500 (1998).
- [49] F. Chevy, V. Bretin, P. Rosenbusch, K. W. Madison, and J. Dalibard, Transverse Breathing Mode of an Elongated Bose-Einstein Condensate, *Phys. Rev. Lett.* **88**, 250402 (2002).
- [50] C. Fort, F. S. Cataliotti, L. Fallani, F. Ferlaino, P. Maddaloni, and M. Inguscio, Collective Excitations of a Trapped Bose-Einstein Condensate in the Presence of a

- 1D Optical Lattice, *Phys. Rev. Lett.* **90**, 140405 (2003).
- [51] L. Yang, X.-R. Wang, Ke Li, X.-Z. Tan, H.-W. Xiong, and B.-L. Lu, Low-Energy Collective Excitation of Bose-Einstein Condensates in an Anisotropic Magnetic Trap, *Chin. Phys. Lett.* **26**, 076701 (2009).
- [52] E. Haller, M. Gustavsson, M. J. Mark, J. G. Danzl, R. Hart, G. Pupillo, and H.-C. Nägerl, Realization of an Excited, Strongly Correlated Quantum Gas Phase, *Science* **325**, 1224 (2009).
- [53] S. E. Pollack, D. Dries, R. G. Hulet, K. M. F. Magalhães, E. A. L. Henn, E. R. F. Ramos, M. A. Caracanhas, and V. S. Bagnato, Collective excitation of a Bose-Einstein condensate by modulation of the atomic scattering length, *Phys. Rev. A* **81**, 053627 (2010).
- [54] T. Kuwamoto and T. Hirano, Collective Excitation of Bose-Einstein Condensates Induced by Evaporative Cooling, *J. Phys. Soc. Jpn.* **81**, 074002 (2012).
- [55] D. S. Lobsenz, A. E. S. Barentine, E. A. Cornell, and H. J. Lewandowski, Observation of a persistent non-equilibrium state in cold atoms, *Nat. Phys.* **11**, 1009 (2015).
- [56] C. J. E. Straatsma, V. E. Colussi, M. J. Davis, D. S. Lobsenz, M. J. Holland, D. Z. Anderson, H. J. Lewandowski, and E. A. Cornell, Collapse and revival of the monopole mode of a degenerate Bose gas in an isotropic harmonic trap, *Phys. Rev. A* **94**, 043640 (2016).
- [57] T. Schumm, S. Hofferberth, L. M. Andersson, S. Wildermuth, S. Groth, I. Bar-Joseph, J. Schmiedmayer, and P. Krüger, Matter-wave interferometry in a double well on an atom chip, *Nat. Phys.* **1**, 57 (2005).
- [58] I. Lesanovsky, S. Hofferberth, J. Schmiedmayer, and P. Schmelcher, Manipulation of ultracold atoms in dressed adiabatic radio-frequency potentials, *Phys. Rev. A* **74**, 033619 (2006).
- [59] G.-B. Jo, Y. Shin, S. Will, T. A. Pasquini, M. Saba, W. Ketterle, D. E. Pritchard, M. Vengalattore, and M. Prentiss, Long Phase Coherence Time and Number Squeezing of Two Bose-Einstein Condensates on an Atom Chip, *Phys. Rev. Lett.* **98**, 030407 (2007).
- [60] J. Fortágh and C. Zimmermann, Magnetic microtraps for ultracold atoms, *Rev. Mod. Phys.* **79**, 235 (2007).
- [61] G. Sinuco-Leon and B. M. Garraway, Radio-frequency dressed lattices for ultracold alkali atoms, *New J. Phys.* **17**, 053037 (2015).
- [62] Y. Colombe, E. Knyazchyan, O. Morizot, B. Mercier, V. Lorent, and H. Perrin, Ultracold atoms confined in rf-induced two-dimensional trapping potentials, *EPL* **67**, 593 (2004).
- [63] K. Merloti, R. Dubessy, L. Longchampbon, A. Perrin, P.-E. Pottie, V. Lorent, and H. Perrin, A two-dimensional quantum gas in a magnetic trap, *New J. Phys.* **15**, 033007 (2013).
- [64] <http://www.zarm.uni-bremen.de/drop-tower.html>
- [65] M. L. Chiofalo, S. Succi, and M. P. Tosi, Ground state of trapped interacting Bose-Einstein condensates by an explicit imaginary-time algorithm, *Phys. Rev. E* **62**, 7438 (2000).
- [66] U. Al Khawaja, C. J. Pethick, and H. Smith, Surface of a Bose-Einstein condensed atomic cloud, *Phys. Rev. A* **60**, 1507 (1999).
- [67] M. M. Cerimele, M. L. Chiofalo, F. Pistella, S. Succi, and M. P. Tosi, Numerical solution of the Gross-Pitaevskii equation using an explicit finite-difference scheme: An application to trapped Bose-Einstein condensates, *Phys. Rev. E* **62**, 1382 (2000).
- [68] M. Cozzini, B. Jackson, and S. Stringari, Vortex Signatures in Annular Bose-Einstein Condensates, *Phys. Rev. A* **73**, 013603 (2006).
- [69] R. Dubessy, T. Liennard, P. Pedri, and H. Perrin, Critical Rotation of an Annular Superfluid Bose-Einstein Condensate, *Phys. Rev. A* **86**, 011602 (2012).
- [70] J. Schneider and A. Schenzle, Output from an atom laser: Theory vs. experiment, *App. Phys. B*, **69**, 353 (1999).
- [71] <https://www.zarm.uni-bremen.de/en.html>